AFRL-AFOSR-UK-TR-2022-0026

Experimental Hypersonic Shock/Boundary-Layer Interaction Studies on a Flat Plate at Elevated Surface Temperature

Alexander Wagner
DEUTSCHES ZENTRUM FUR LUFT- UND RAUMFAHRT E.V.
LINDER HOHE
KOLN, NORDRHEIN-WESTFALEN, 51147
DEU

03/02/2022
Final Technical Report

Air Force Research Laboratory
Air Force Office of Scientific Research
European Office of Aerospace Research and Development
Unit 4515 Box 14, APO AE 09421

REPORT DOCUMENTATION PAGE

PLEASE DO NOT RETURN YOUR FORM TO THE ABOVE ORGANIZATION.

1. REPORT DATE	2. REPORT TYPE	3. DATES COVERED	
20220302	Final	START DATE 20161115	END DATE 20211114

4. TITLE AND SUBTITLE
Experimental Hypersonic Shock/Boundary-Layer
Interaction Studies on a Flat Plate at Elevated Surface Temperature

5a. CONTRACT NUMBER	5b. GRANT NUMBER	5c. PROGRAM ELEMENT NUMBER
	FA9550-17-1-0060	61102F
5d. PROJECT NUMBER	**5e. TASK NUMBER**	**5f. WORK UNIT NUMBER**

6. AUTHOR(S)
Alexander Wagner

7. PERFORMING ORGANIZATION NAME(S) AND ADDRESS(ES)
DEUTSCHES ZENTRUM FUR LUFT- UND RAUMFAHRT E.V.
LINDER HOHE
KOLN, NORDRHEIN-WESTFALEN 51147
DEU

8. PERFORMING ORGANIZATION REPORT NUMBER

9. SPONSORING/MONITORING AGENCY NAME(S) AND ADDRESS(ES)	10. SPONSOR/MONITOR'S ACRONYM(S)	11. SPONSOR/MONITOR'S REPORT NUMBER(S)
EOARD UNIT 4515 APO AE 09421-4515	AFRL/AFOSR IOE	AFRL-AFOSR-UK-TR-2022-0026

12. DISTRIBUTION/AVAILABILITY STATEMENT
A Distribution Unlimited: PB Public Release

13. SUPPLEMENTARY NOTES

14. ABSTRACT
Shock wave/boundary layer (SWBLI) experiments in a hypersonic flow with highly cooled walls at varying wall-to-freestream temperature ratios were successfully carried out at the High Enthalpy Shock Tunnel Gottingen (HEG).

In the scope of the activity a flat plate model was modified to accommodate an improved electrical surface heating technique and to realize an increased spatial density of surface-mounted
transducers for surface heat flux and pressure measurements. The wind tunnel model was designed to reach up to 800 K which marks the limits of the high temperature instrumentation. A shock generator subsystem was designed to be installed above the flat plate model in order to generate an impinging a shock wave onto the heated flat plate surface. The generated shock interacts with an incoming turbulent boundary layer which was tripped to ensure a fully turbulent boundary layer in a repeatable way. The resultant SWBLI was visualized with conventional and focused schlieren optical diagnostics.

Results show that an increasing impinging shock angle increases the size of the separation region, which is in accordance with the accompanied LES results conducted by the group of Prof. Johan Larsson (Uni Maryland). The effect of varying wall-to-freestream temperatures were investigated in a range of Tw=Tinf = 1.14 to Tw=Tinf = 2.70 keeping the free-stream conditions constant while varying the surface temperature of the wind tunnel model. An increasing wall temperature was found to lead to an increased SWBLI interaction length. Furthermore, an impact on the surface heat flux relaxation after the shock impingement was observed.

15. SUBJECT TERMS

16. SECURITY CLASSIFICATION OF:			17. LIMITATION OF ABSTRACT	18. NUMBER OF PAGES
a. REPORT	b. ABSTRACT	c. THIS PAGE		
U	U	U	SAR	43

19a. NAME OF RESPONSIBLE PERSON	19b. PHONE NUMBER *(Include area code)*
DOUGLAS SMITH	314 235 6013

DLR IB-XXX

Hypersonic Shock Wave Boundary Layer Interaction Experiments on a Flat Plate at Elevated Surface Temperature

FINAL REPORT

DLR

Document properties

Title	Hypersonic Shock Wave Boundary Layer Interaction Experiments on a Flat Plate at Elevated Surface Temperature
Subject	FINAL REPORT
Project Type	Grant/Cooperative Agreement Award
PI	Dr. Alexander Wagner (DLR-GO)
Coauthors	Dr. Divek Surujhlal (DLR-GO)
Grant Number	FA9550-17-1-0060
Period	15.11.2016 to 14.11.2021
Date	February 28, 2022
Version	1.0
File Path	FinalReport

Contents

1. Preface

The present study has been initiated as a closely coupled research activity with Professor Johan Larsson of University of Maryland (USA). His AFOSR grant on 'The effects of strong wall cooling on supersonic and hypersonic shock/boundary-layer interactions' addressed the scientific subject using wall-modeled large eddy simulations. The results of the numerical work were used to support the wind tunnel design process of the present study. The main purpose of the joint venture was to investigate a specific fluid dynamic problem numerically and experimentally using the same model setup and free-stream conditions. As a result the present study provides experimental data which were gathered using boundary conditions as close as possible to the numerical setup, i.e. using the same shock generator angles, wall temperature ratios, free-stream conditions and boundary layer state for example.

2. Summary

Shock wave/boundary layer (SWBLI) experiments in a hypersonic flow with highly cooled walls at varying wall-to-freestream temperature ratios were successfully carried out at the High Enthalpy Shock Tunnel Göttingen (HEG).

In the scope of the activity a flat plate model was modified to accommodate an improved electrical surface heating technique and to realize an increased spatial density of surface-mounted transducers for surface heat flux and pressure measurements. The wind tunnel model was designed to reach up to 800 K which marks the limits of the high temperature instrumentation. A shock generator subsystem was designed to be installed above the flat plate model in order to generate an impinging a shock wave onto the heated flat plate surface. The generated shock interacts with an incoming turbulent boundary layer which was tripped to ensure a fully turbulent boundary layer in a repeatable way. The resultant SWBLI was visualized with conventional and focused schlieren optical diagnostics.

Results show that an increasing impinging shock angle increases the size of the separation region, which is in accordance with the accompanied LES results conducted by the group of Prof. Johan Larsson (Uni Maryland). The effect of varying wall-to-freestream temperatures were investigated in a range of $T_w/T_\infty = 1.14$ to $T_w/T_\infty = 2.70$ keeping the free-stream conditions constant while varying the surface temperature of the wind tunnel model. An increasing wall temperature was found to lead to an increased SWBLI interaction length. Furthermore, an impact on the surface heat flux relaxation after the shock impingement was observed.

3. Introduction

3.1. Shockwave/boundary layer interactions (SWBLIs)

A shockwave/boundary-layer interaction (SWBLI) occurring within a flow can be a critical factor in determining the performance of a vehicle or a propulsion system. SWBLIs occur on external or internal surfaces causing intense adverse pressure gradients in the boundary layer imposed by the shock. The adverse pressure gradient distorts the boundary layer profile causing it to become less full. If the shock is strong enough, the boundary layer separates which can lead to dramatic changes in the entire flow field structure with formation of intense vortices or complex shock patterns. In addition, shock-induced separation may cause large-scale unsteadiness leading to e.g. air-intake disturbances and unsteady aerodynamic loads. Consequently, uncontrolled SWBLIs are likely to limit the performance of a vehicle and, if strong enough, may cause structural damage, Babinsky and Harvey (2011).

During the last decades our understanding of SWBLIs and our ability to predict these flows have advanced significantly. However, most of the experimental and numerical work concentrated on cases with nearly adiabatic wall, i.e. where the wall temperature T_w is close to the recovery temperature T_r of the incoming boundary layer, see for example, Schülein (2014), Law (1976), Horstman (1992), Sandham et al. (2014). This is problematic, since a cooled wall, i.e. $T_w < T_r$, can have a very large effect on an SWBLI. Despite having identical free-stream conditions and incoming shock strength, the differences in the SWBLI can be striking. Only a number of experimental studies with cooled wall conditions are available. These studies are typically conducted in shock tunnels taking advantage of the high total temperatures while leaving the model at ambient temperature with little temperature increase over test time, see for example, Sandham et al. (2014); Holden (1972, 1978). The variation of the ratio T_w/T_r in these test facilities is usually realized by choosing test conditions with different total temperatures. This in turn causes large variations in the free-stream conditions preventing a direct study of wall temperature effects on SWBLIs. To isolate the effect of varying temperature ratios it is desirable to keep the free-stream test conditions constant while changing the model wall temperature. This can be realized by e.g. using liquid nitrogen for cooling as reported in Lewis et al. (1967) or by heating the wind tunnel model as reported in Bleilebens and Olivier (2006) and Scortecci et al. (1998). Since heating and cooling techniques involve an enormous increase of the complexity of experimental setup very few experimental data for CFD validation are available.

The present study aims for the experimental investigation of shock/boundary-layer interactions on a flat plate model with an impinging shock wave and variable surface temperature in the High Enthalpy Shock Tunnel Göttingen (HEG). Results for ambient, medium and high surface temperatures will be elaborated. This study will support the companion proposal by providing experimental results to improve the physical understanding of the effects of

wall cooling. The proposed tests in HEG offer the opportunity to extend the study towards hypervelocity conditions and a limited study under high-enthalpy conditions was additionally undertaken during this project.

3.2. Relevance of the joined LES simulations

Volpiani Volpiani et al. (2019) provides an overview on the large-eddy simulations of an impinging shock interaction with a turbulent boundary layer conducted in the scope of the joined AFOSR research grant as described in chapter 1. The simulations were performed at nominal HEG conditions assuming two different wall temperature to recovery temperature ratios of $T_w/T_r = 0.33$ and $T_w/T_r = 0.13$. The Reynolds numbers based on the boundary layer thickness and the momentum thickness at the shock impingement location, δ_0 and θ_0 , were defined as $Re_\delta = \rho_\infty u_\infty \delta_0/\mu_\infty$ and $Re_\theta = \rho_\infty u_\infty \theta_0/\mu_\infty$. Table 3-1 lists the corresponding conditions.

Simulation	Re_δ	Re_θ
BL-0.13	47420	2045
BL-0.33	49406	1802

3-1 Global characteristics of the turbulent boundary layers at shock impingement locations.

The flow parameters for the SWBLI simulations at free-stream Mach number $M_\infty = 7.4$ and wall-to-recovery-temperature ratio T_w/T_r, incidence angle of the shock generator ϕ and the length of the recirculation bubble L_{sep} are shown in table 3-2.

Simulation	T_w/T_r	ϕ [°]	T_w/T_∞	L_{sep}/δ_0
SBLI-0.33-12	0.33	12	2.77	1.2
SBLI-0.33-15	0.33	15	2.77	3.3
SBLI-0.33-18	0.33	18	2.77	5.5
SBLI-0.33-24	0.33	24	2.77	9.6
SBLI-0.13-12	0.13	12	1.12	0.6
SBLI-0.13-15	0.13	15	1.12	1.8
SBLI-0.13-18	0.13	18	1.12	3.9

3-2 Flow parameters of the LES SWBLI simulations.

Figure 3-1 provides an excellent overview on the flow topology of the SBLI with different shock angles and wall temperatures in terms of skin friction, heat flux, wall pressure and wall pressure fluctuations. The most important findings can be summarized as follows.

- the skin friction distributions are rather similar for the two wall temperatures upstream of the interaction region

- the mean wall pressure and the mean wall pressure fluctuations obtained for each wall temperature collapse surprisingly well for each shock strength
- shock strength and wall temperature affect the separation location, but have little influence on the reattachment position (in the normalized x-axis)
- the skin friction oscillates between positive and negative values in the separation zone making the definition of the separation length more challenging compared to lower Mach number cases.

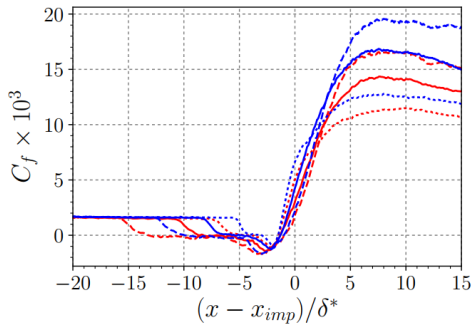

(a) Distribution of the mean skin friction coefficient

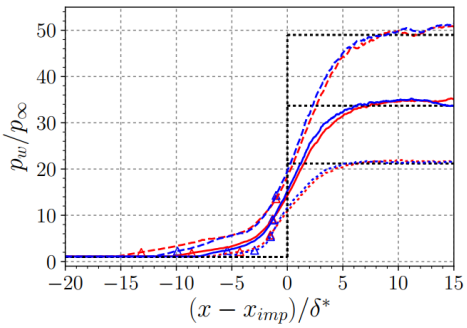

(b) Distribution of the mean wall pressure

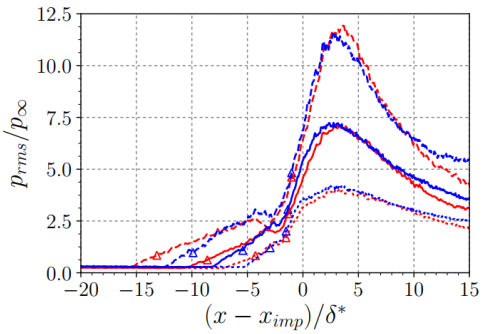

(c) Distribution of the root-mean-square wall pressure

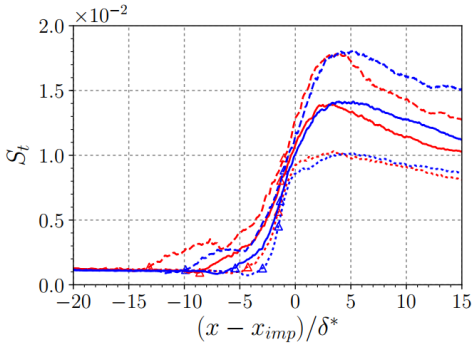

(d) Distribution of the mean Stanton number

3-1 Mean flow properties across the interaction zone at two wall-to-recovery-temperature ratios: $T_w/T_r = 0.33$ (red) and $T_w/T_r = 0.13$ (blue) and different deflection angles: $\phi = 12\,\mathrm{deg}$ (dotted), $\phi = 15\,\mathrm{deg}$ (solid) and $\phi = 18\,\mathrm{deg}$ (dashed lines). Triangles indicate the separation and reattachment position. Note that the x-axis is normalized by the boundary layer displacement thickness δ^*.

The above data is considered to be the essence of the numerical investigations. It remains a challenge to connect and compare the experimentally and numerically obtained data. In experiments physical parameters such as boundary layer displacement thickness or momentum thickness are not accessible. However, these parameters are often used for normalization. In the present study we spent the effort to extract the mean boundary layer thickness out of post-processed schlieren images. However, as schlieren techniques visualize density gradients which are strongly influenced by the thermal boundary layer, it needs to be considered that a boundary layer thickness based on the velocity is not identical with a density gradient based boundary layer thickness. We will address this point later again.
For future work (not in the scope of the present project) we plan conducting RANS com-

putations at the experimental test conditions trying to match the tripped boundary layer thickness observed. Based on these computation missing parameters such as momentum thickness could be extracted.

4. Experimental Setup

4.1. Overview of model configuration

The complete wind tunnel model configuration is shown in figure 4-1. The model consists of two subsystems:

1. the flat plate
2. the shock generator.

These are labeled in figure 4-1. The purpose of the flat plate was to provide a surface on which a turbulent boundary layer was developed. Furthermore, it provided a surface onto which the shock wave could impinge, thereby interacting with the incoming turbulent boundary layer and creating a turbulent SWBLI on the surface. The upstream portion

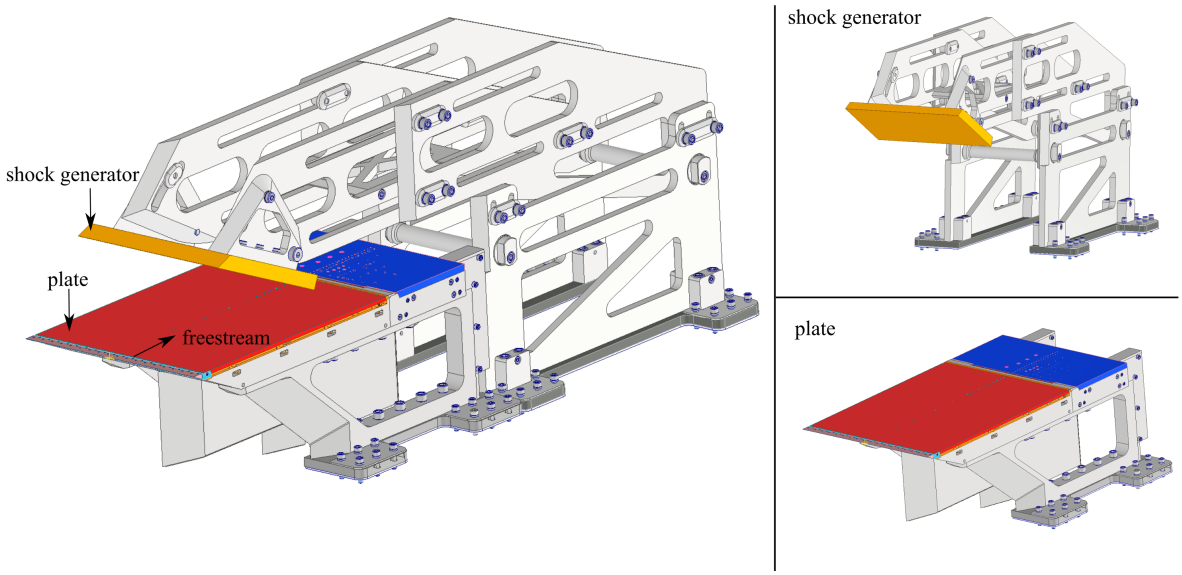

4-1 Overview of wind tunnel model and its subsystems.

(colored red in figure 4-1) could be electrically heated to a maximum surface temperature of 714 K at vacuum conditions. The exchangeable leading edge was passively heated due to heat conduction. The downstream portion (colored blue) was left unheated to accommodate a higher spatial density of standard surface-mounted transducers.

The purpose of the shock generator was to create a shock wave which imparted a pressure rise to the incoming turbulent boundary layer on the plate. The magnitude of the pressure gradient was varied based on the angle of the shock generator plate, shown in orange in figure 4-1. Different shock generator angles were used during the experiments. The mechanical design of these subsystems was detailed in a previous project report. The design

process included finite element computations to ensure a stiffness of the assembly large enough to keep the shock generator in place despite the enormous forces acting on in during a test. The model is shown as installed in the test section of HEG in figure 4-2

4-2 Flat plate and shock generator installed in the test section of the High Enthalpy Shock Tunnel Göttingen.

4.2. Flat plate leading edge

The leading edge of the plate was exchangeable. Four different leading edge types were used:

1. a blunt leading edge of nominal radius $R_n = 0.1\ mm$
2. a sharp leading edge (broken off)
3. a sharp leading edge with screws and gravel as roughness elements on the plane surface
4. a sharp leading edge with distributed roughness elements on the plane surface.

The blunt leading edge was used to obtain a laminar boundary layer. This offers a stable surface heat flux and pressure distribution and was used to ensure that the surface-mounted transducers were in functional.

The sharp leading edge was used to test the natural boundary layer development on the flat plate in order to assess the need to artificially trip the boundary layer to ensure turbulence. Artificial tripping of the boundary layer was indeed required as a fully developed

natural turbulent boundary layer was not reached at the highest free-stream unit Reynolds number test condition. This necessitated the use of leading edges with roughness elements.

For completeness, the stepped interface between the leading edge piece and the heated portion of the flat plate was measured. This was done by traversing a Mitutoyo Surftest SJ-410 gauge profilometer across the step to measure the height increase (backwards facing step) from the leading edge to the heated portion. The profilometer was calibrated with a $Ra = 3.000\ \mu m$ specimen. The results of step height along the span of different leading edges are shown in figure 4-3. In conclusion, the remaining step height at the interface is not expected to have a significant effect since the step is small compared to the roughness heights and since it is facing backwards.

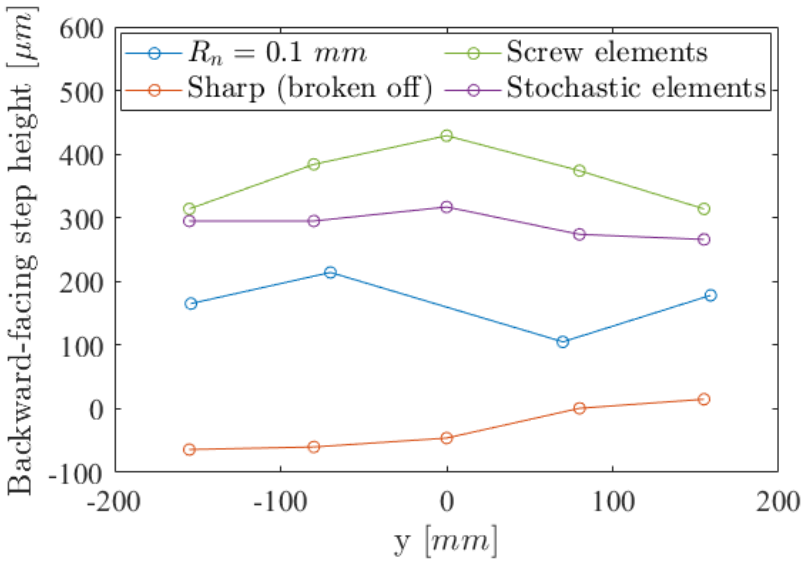

4-3 Backward-facing step heights along the span of the flat plate model for different leading edges. Leading edge types are indicated in the legend. Measurements were made with the Mitutoyo Surftest SJ-410 gauge profilometer across the step. Positive step heights indicate backwards-facing steps. Negative step heights indicate forward-facing step heights.

4.3. Roughness elements

Two types of roughness element configurations were applied to the leading edg of the flat plate. Type 1 consists of staggered M4 screws with gravel interspersion. Type 2 consists of interspersed gravel. Their profiles were each scanned with a laser profilometer. The scan CONTROL 2900-100 BL laser profilometer from Micro-Epsilon was used. The emitter used had a 405 nm laser diode with $8\ mW$ power output. The resolution in the streamwise direction was fixed by the manufacturer at 1280 points per profile. Physical resolution was determined by the combination of the line sampling rate of 59 Hz and traverse speed in the $y-$coordinate set at $83 \pm 8\ \mu m/s$. Angular offset of the profilometer beam relative to the leading edge surface and the distance from the laser diode to the surface were suitably

minimised to increase resolution and resultant profile signal integrity. The resolution in the three coordinate axes obtained is given in Table 4-1.

4-1 Profilometer resolution specifications. The number of points comprising the smallest roughness element is detailed in the final column for a smallest element size of $0.4\ mm$.

Coordinate	Mean resolution [$\mu m \pm 0.1 \mu m$]	Points per smallest element
x	65.0	6
y	9.3	44
z	6.4	62

The setup used is shown in figure 4-4.

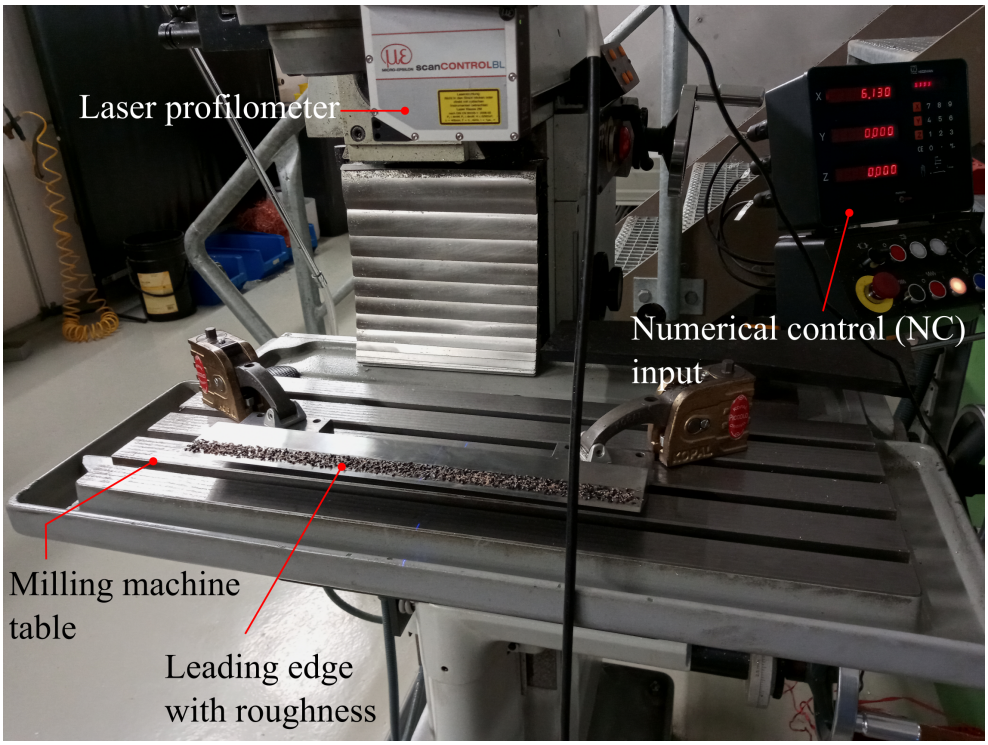

4-4 Overview of profilometer setup on a numerical control (NC) milling machine. The profilometer was fixed with the tool head of the milling machine and programmed to translate from right to left as shown in the figure. In this way, scans could be made of the leading edge roughness elements placed on the table of the milling machine.

Scans obtained from the profilometer were analysed for height variations (h) as well by obtaining the in-plane extents of the roughness elements with an image analysis technique (as if viewing the roughness elments from above). A probability exceedance curve was obtained for these two methods, which is shown for each roughness type in figure 4-5. The 30^{th}-percentile vertical height and in-plane extents correspond closely. Therefore the vertical height was used as the representative roughness element height k_{30}. The use of the 30^{th}-percentile vertical height is justified in the works of Reda (1981), Batt and Legner (1983) and Reda (2002). Roughness elements as applied on the exchangeable leading edge

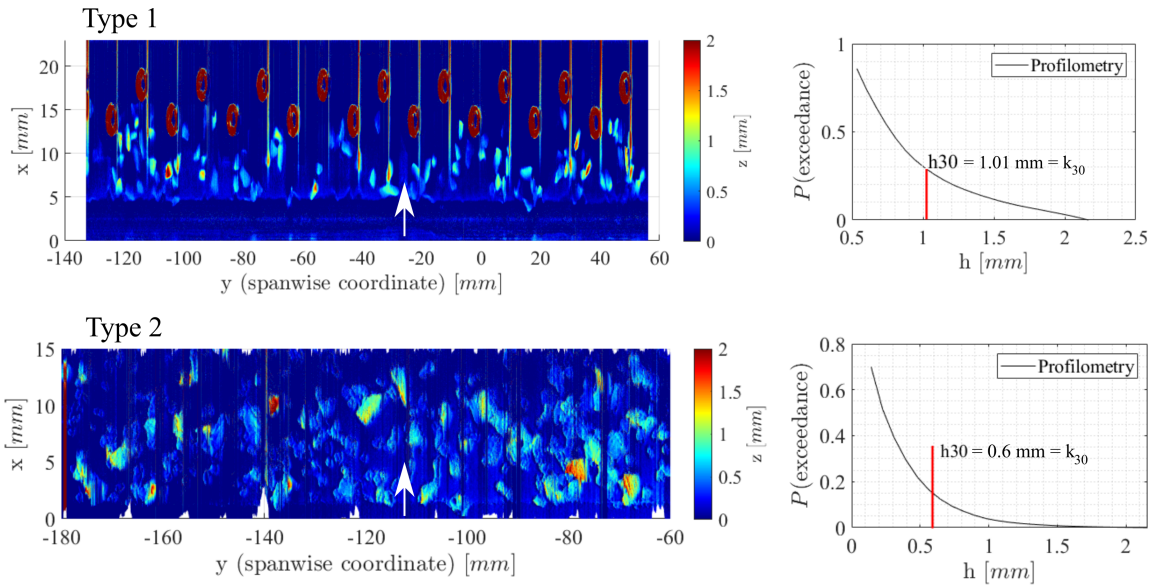

4-5 Overview of the two leading edge roughness elements used on the flat plate. Type 1 consists of staggered M4 screws with gravel interspersion. Type 2 consists of interspersed gravel. The 30^{th}-percentile vertical height and in-plane extents corresponded closely, therefore the vertical height was used as the representative roughness element height k_{30}.

surfaces are shown in figure 4-6 for both types of roughness.

4.4. Flat plate heating

The flat plate was comprised of two portions. The plate between streamwise coordinates $x = 20\ mm$ and $x = 487\ mm$ was equipped with two $3000\ W$ heating elements - one on either side of the centerline. The portion between $x = 487\ mm$ and $x = 686.6\ mm$ is left unheated. The heated portion required pressure and temperature transducers with high-temperature-resistant properties with increased costs per transducer. Six Type K Medtherm thermocouples were installed on the heating element to measure its temperature (called the control temperature). The temperature of the heating element was regulated with a proportional-integral-derivative (PID) controller. Two control temperatures, 400 $°C$ and 500 $°C$, were used for these tests. An infrared (IR) camera (thermoIMAGER from MicroEpsilon) with a resolution of 288×382 pixels was used to obtain the two-dimensional temperature distribution on the plate as a result of heating. The surface was painted black to increase the emissivity for the IR calibration. Locations with transducers such as the centerline of the heated portion as well as on the unheated portions were left unpainted from which temperature could not be inferred from the IR measurements. Furthermore, the field-of-view of the IR-camera was not large enough to capture the entire plate in a single frame. Therefore, multiple images were recorded (3 per temperature setting) and stitched together. The 2D temperature distributions for medium and high control temperatures are shown in figure 4-7. Note the different limits on the color bars. This emphasizes the repeatable surface temperature distributions at different control temperatures.

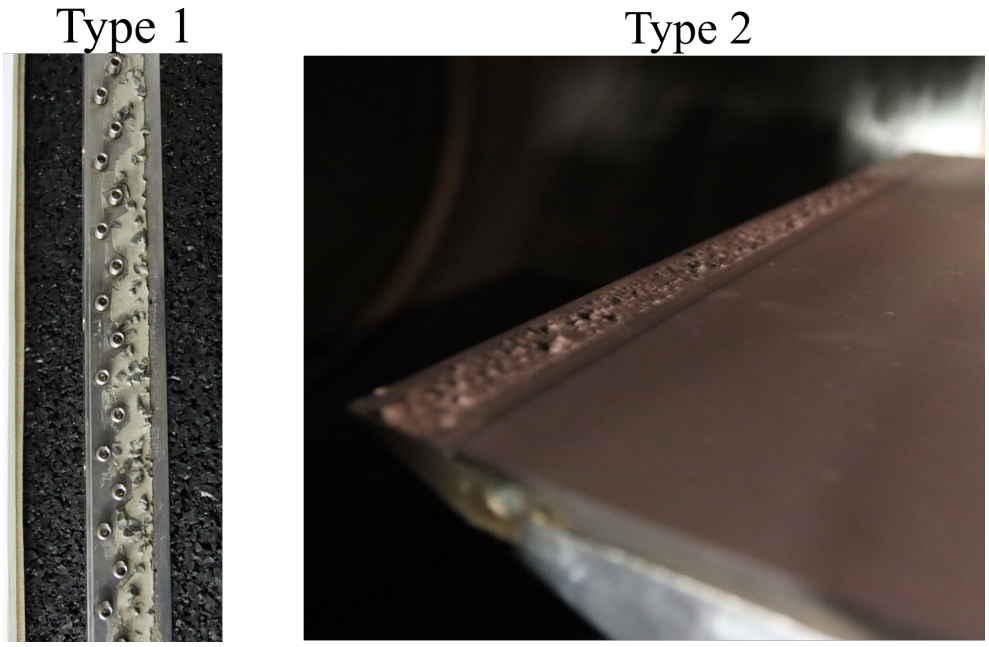

4-6 Photographs of the leading edge roughness elements as applied. Type 1 consists of staggered M4 screws with gravel interspersion. Type 2 consists of interspersed gravel.

Quantification of the temperatures in the spanwise direction of the flat plate are shown in figure 4-8. A maximum temperature of 714 K was reached for a control temperature of 773 K. The temperature reduces towards the side edges and leading edge of the plate due to unavoidable conduction losses through these surfaces and radiation to the surroundings. The unheated portion was well isolated from the heated portion with significant temperature reduction near this region as indicated. This was important to the functioning of the sensors placed on this portion.

Additional preliminary work was done to ensure the flatness of the plate surface once control temperatures were reached and held constant. This was assessed with a straight rule placed on the surface, as shown in figure 4-9.

4.5. Flat plate instrumentation

The heated portion required transducers with high-temperature-resitant properties with increased costs per transducer. The unheated portion could therefore be equipped with a higher spatial density of standard transducers and was targeted for a detailed investigation of the SWBLI region. The instrumentation layouts of the heated and unheated portions are shown on the left and right of figure 4-10, respectively.

Pressure sensors were calibrated once installed in the model in the test section. Sensitivies were recorded between pressures of $0.1\ mbar$ to $800\ mbar$ for an unheated flat plate, and between $416\ mbar$ to $937\ mbar$ for a control temperature of $500°\ C$ on the heated portion. Sensitivities between unheated and heated calibrations differed by approximately 15% for the pressure sensors on the unheated portion of the plate and by less than 2% for the

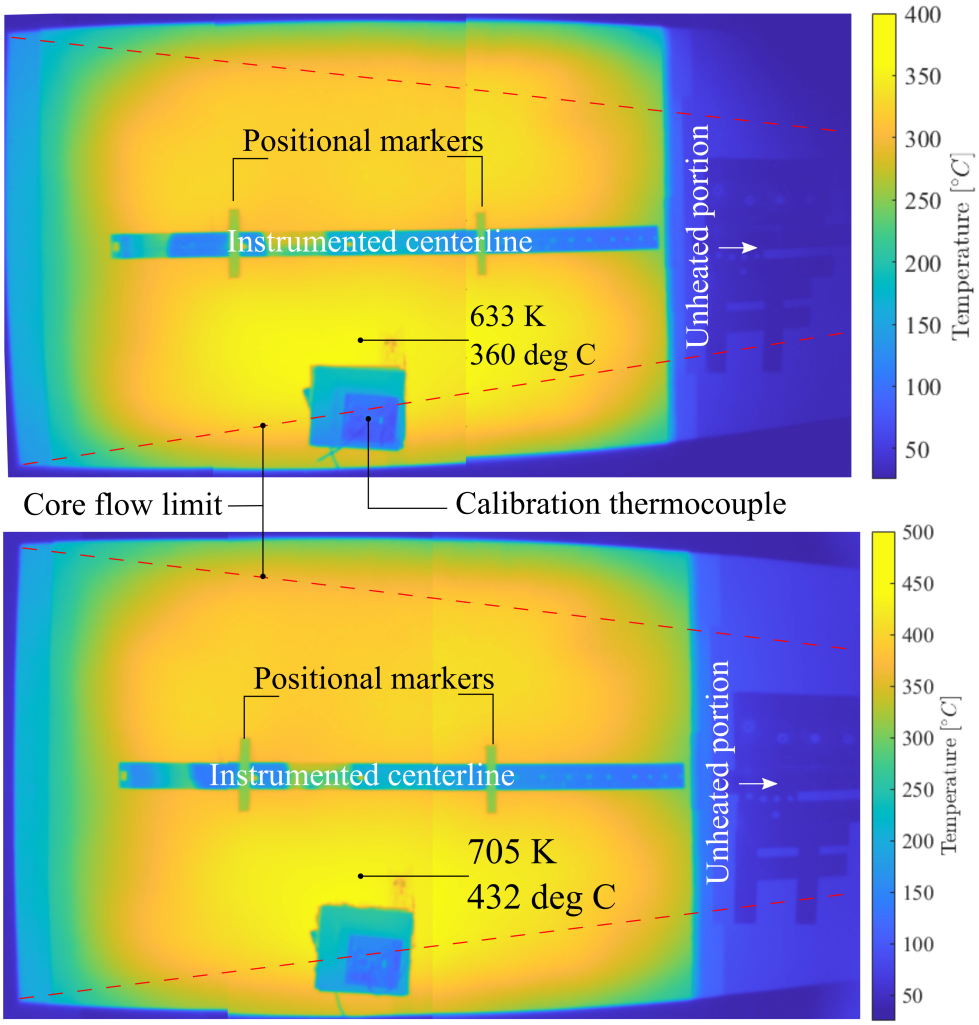

4-7 Temperature distribution for a control temperature of 400 $^{\circ}C$ (top) and 500 $^{\circ}C$ (bottom) control temperatures. Colour bars have different ranges to reflect the repeatability of temperature distributions as different control temperatures. Positional markers were used as references when stitching the IR images together.

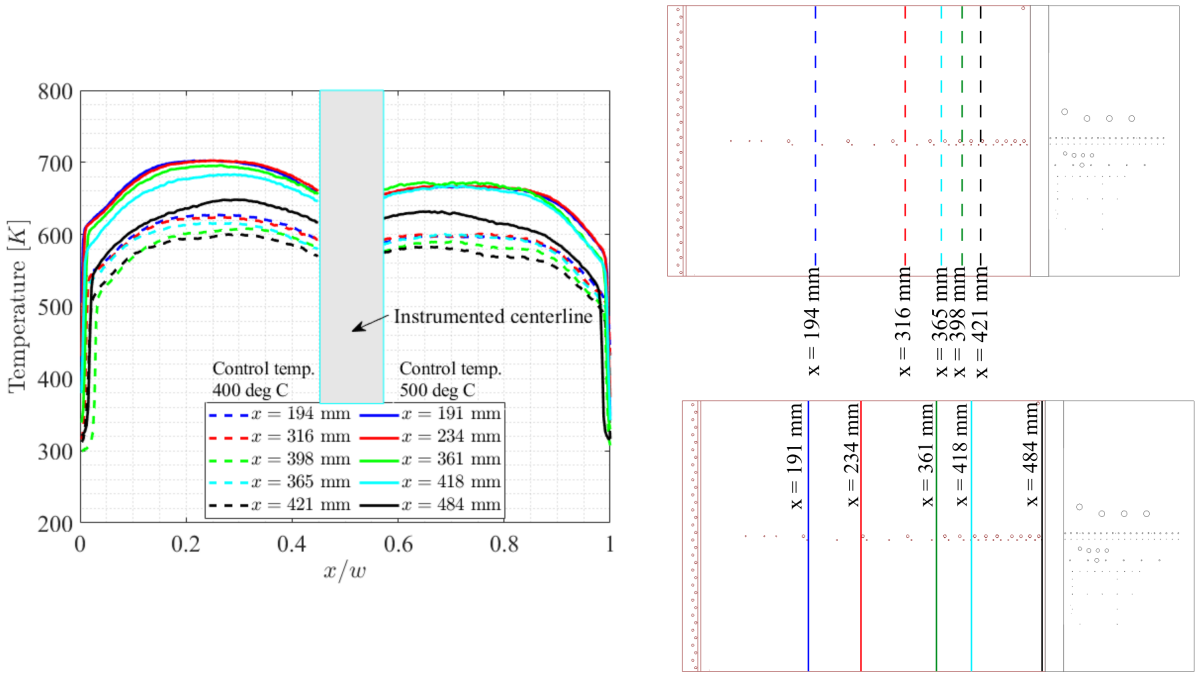

4-8 Spanwise temperature distribution along the flat plate model at different streamwise locations. Dotted lines refer to spanwise temperature profiles for a control temperature of $400^\circ\ C$. Solid lines refer to spanwise temperature profiles for a control temperature of $500^\circ\ C$.

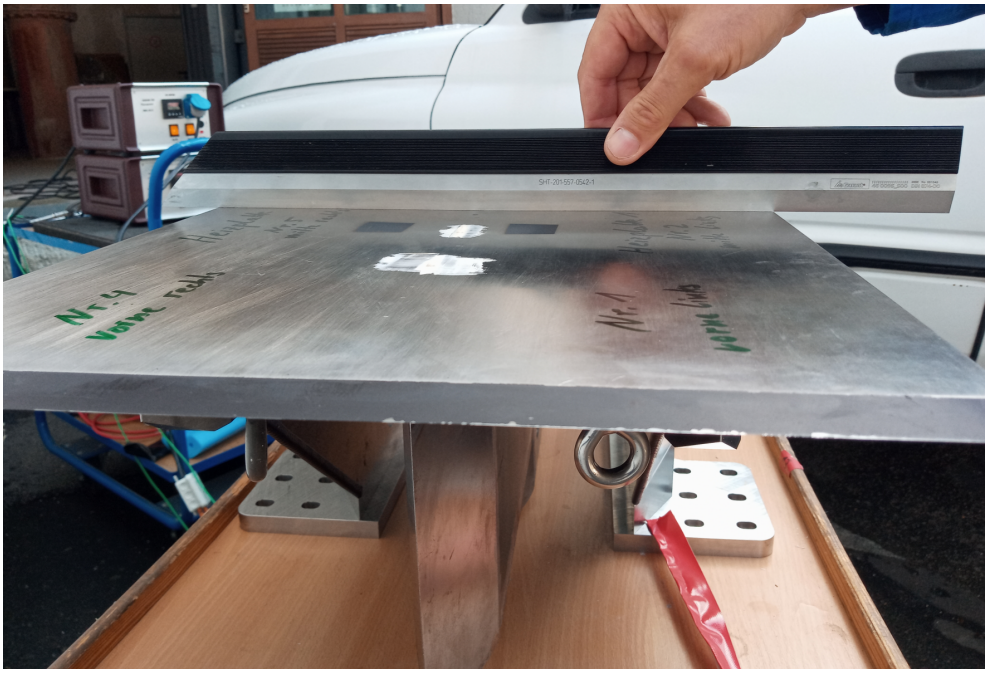

4-9 Preliminary tests to ensure plate surface flatness with a straight rule after the control temperature was reached and held stable as done during HEG tests.

pressure sensors on the heated portion.

4.6. High speed optical diagnostics

4.6.1. Schlieren

A classical Z-type schlieren system (as referenced by Settles (2001)) was setup with a Cavilux laser (from Cavitar $690 \pm 10\ nm$ wavelength with a power rating of $400\ mW$). A Phantom v2012 high-speed camera was used for image acquisition with a frequency of $75\ kHz$ and a resolution of 1024×272 pixels for the the runs with SWBLIs.

4.6.2. Focused schlieren

A focused schlieren system was set up in order to overcome the path-integration property of the conventional schlieren system. This is especially relevant for models with large spans, such as the flat plate used in this work, and tunnels with strong nozzle shear layers. A schematic of the setup is shown in figure 4-11. The operating principal of the focused schlieren relies on the combined use of a source/cutoff grids and an objective lens. The grids provide a multiple source and cutoff arrangement Weinstein (2010). The image is therefore formed from a superposition of component schlieren images resulting from the source/cutoff grid pairs. This assists the amplification of features common to all sources and averaging out of features which are not. The placements of the source and cutoff grids were based on practical considerations regarding available optical table and access for fine adjustments.

The objective lens aperture determines the focusing ability of the system Weinstein (1993). Its distance from the density object (i.e.the plane of interest on the flat plate model) was determined by the formation of the source grid image at the cutoff grid. The cutoff grid was a photographic negative of the source grid such that fine vertical adjustment of the cutoff grid served to adjust the system sensitivity, as is done in a conventional schlieren setup. Fresnel lenses have been recommended in the past for improved brightness. However, a Cavilux laser (from Cavitar $690 \pm 10\ nm$ wavelength with a power rating of $400\ mW$) used at $10\ ns$ pulsewidth was able to provide enough image brightness for the sensitivity settings chosen for image acquisition. A Phantom v2012 high-speed camera was used for image acquisition with a frequency of $42\ kHz$ and a resolution of 1152×464 pixels for the the runs with SWBLIs.

4.7. Overview of test matrix

The parameters to be varied over the course of the experiments are listed below:

1. leading edge type (including roughness type)
2. surface temperature
3. shock generator angle.

Furthermore, 2 free-stream conditions were tested. Freetsream conditions are detailed in table 4-4. 21 runs comprised Condition A, and 1 run was at Condition B.

Three surface temperatures were chosen to investigate SWBLIs. This is classified in table 4-2. The nomenclature used will refer to the temperature ratio T_w/T_∞ as used in section 3.2. This is based on the free-stream temperature of Condition A.

4-2 Definition of plate surface temperatures chosen for investigation of SWBLIs.

Name	T_w	T_w/T_∞
Low	$300\ K$	1.14
Medium	$633\ K$	2.40
High	$714\ K$	2.70

4.7.1. Reservoir and free-stream conditions

Mean reservoir conditions over 21 tunnel runs at the same nominal conditions showed minimal standard deviations of reservoir test gas properties. There were therefore minor run-to-run variations in the boundary layer properties of the flat plate, for a given model leading edge and wall temperature distribution. Reservoir variations resulted in small standard deviations in the properties of the free-stream, which are shown in table 4-4 for 21 runs at condition A and for a single run at condition B.

4-3 Mean stagnation properties of the HEG based on 21 runs at condition A. $\rho_{0,CEA}$ was calculated using the NASA Chemical Equilibrium with Applications (CEA) databases.

$p_0\ [Pa]$	29.05 $\pm 1.15\%$
$T_0\ [K]$	2658.4 $\pm 0.99\%$
$h_0\ [MJ/kg]$	3.14 $\pm 1.19\%$
$\rho_{0,CEA}\ [kg/m^3]$	37.9 $\pm 1.44\%$

4-4 Mean free-stream properties of the HEG based on 21 runsat Condition A. Data for a single run at Condition B is included. All properties were extracted from non-equilibrium nozzle computations in the DLR-TAU code (Mack and Hannemann, 2002).

	Condition A	Condition B
$p_\infty\ [Pa]$	3444.7 $\pm 1.19\%$	2299.7
$T_\infty\ [K]$	264.26 $\pm 1.35\%$	277.26
$u_\infty\ [m/s]$	2387.7 $\pm 0.53\%$	2429.2
$\rho_\infty\ [kg/m^3]$	0.0452 $\pm 1.45\%$	0.0288
$Re_u\ \times 10^{-6}\ [m^{-1}]$	6.47 $\pm 1.86\%$	4.03

4.7.2. Overview of SWBLI test cases for relation with LES

In order to link the current experiments with LES computations, the information contained in tables 3-1 and 3-2 would ideally be used to re-compute the experimental test cases. As mentioned in section 3.2, not all parameters could be easured in experiments. The LES-relevant parameters therefore have to be extracted from what was achieveable from measurements but then also require proper specification so as to facilitate cooperation with LES practices.

In this sense, temperature ratios T_w/T_∞ is used for temperature ratio specification, with T_∞ extracted from non-equilibrium RANS nozzle simulations carried out in the DLR-TAU code. The parameter δ_0 used in the LES was defined as the velocity boundary layer thickness. From experiments, schlieren visualisations were used to obtain the density-gradient-based boundary layer thickness δ_ρ, which can be up to 50% larger than the velocity-based boundary layer thickness as found in previous studies. This meant that parameters L_{sep}/δ_ρ and $Re_{\delta\rho}$ could be additionally quantified. For all cases with SWBLIs, LES-relevant flow parameters are shown in table 4-5.

4-5 LES-relevant parameters as per table 3-2 extracted experimental results for Condition A.

T_w/T_∞	$\phi\ [^\circ]$	L_{sep}/δ_ρ	$Re_{\delta\rho}$
2.45	12	4.28	9.42×10^4
2.42	12	3.66	9.49×10^4
2.39	18	9.90	9.21×10^4
2.74	9	5.59	9.55×10^4
2.81	12	4.41	9.68×10^4

TH : Medtherm Type E high-temp. resistant thermocouples
PH : Kulite high-temp. resistant pressure sensors (240 kHz resonant frequency)
TC and TCA : Medtherm Type E thermocouples
GE, GEA - GEF : GE NPP 301 pressure sensors
ALTP : Atomic layer thermopiles for high frequency (< ~500kHz) heat flux
PCB : Piezoelectric pressure transducers (11 kHz - 1 MHz) types A31, A37, B38

4-10 Surface-mounted sensors used on the heated (left) and unheated portions (right) of the flat plate. Further details of the instrumentation used can be found in the appendices.

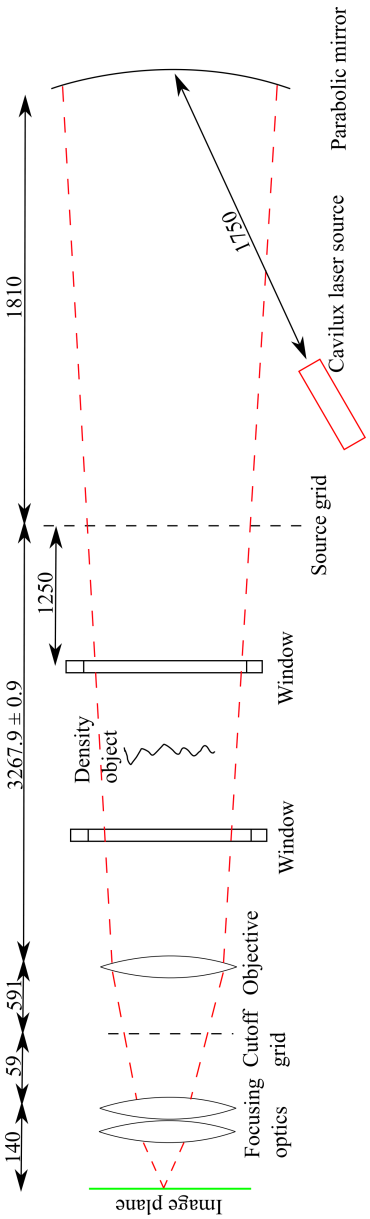

4-11 Schematic of the focused schlieren layout used during experiments. All dimensions in mm. Not to scale.

5. Results

5.1. Effect of leading edge radius (without roughness)

Two different leading edges (one sharp and one with a specified bluntness) were examined to investigate if a natural turbulent boundary layer was achievable on the flat plate. The blunted leading edge had a radius of $R_n = 0.1\ mm$, as measured with the Hexagon Global DEA 7-10-7 coordinate measuring device. The impact of the leading edge (LE) radius on mean surface heat flux is shown in figure 5-1.

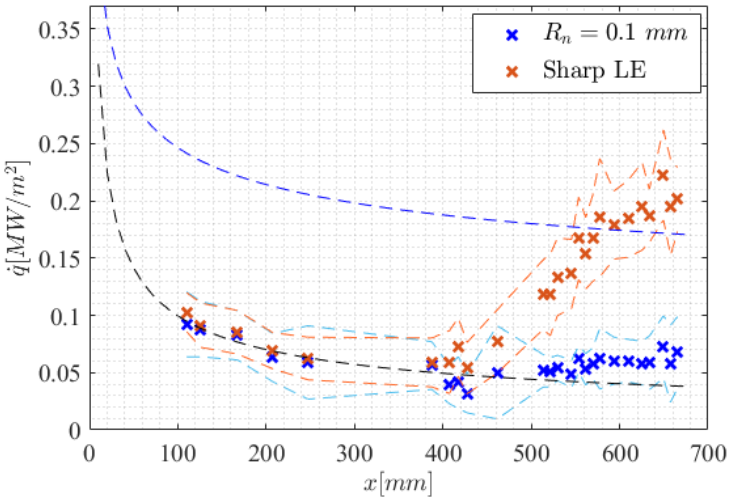

5-1 Mean surface heat flux along the centerline of the plate at $T_w = 300\ K$ with a sharp and blunt ($R_n = 0.1\ mm$) leading edges. Standard deviation limits are indicated by the translucent dotted lines. The solid black and blue dotted lines correspond to the local laminar and turbulent surface heating as per the models of van Driest (1956).

With the sharp leading edge, significantly higher mean surface heat flux was achieved towards the downstream end of the plate. However, a fully established turbulent boundary layer required for the turbulent SWBLI was not evident. This justified the need for tripping the boundary layer to obtain a turbulent SWBLI.

5.2. Roughness-induced turbulent boundary layers

5.2.1. Effect of roughness type

An extensive preliminary experimental programme on roughness-induced transition was initiated during the manufacture and instrumentation of the current model. The results of this preliminary programme were detailed in previous interim reports. This informed the current study in terms of roughness types and dimensions to select in order to obtain

a turbulent boundary layer as far upstream on the plate as possible, whilst minimising perturbations to the outer free-stream flow.

A comparison between the mean surface heat flux along the plate centerline for two different types of leading edge roughness is shown in figure 5-2.

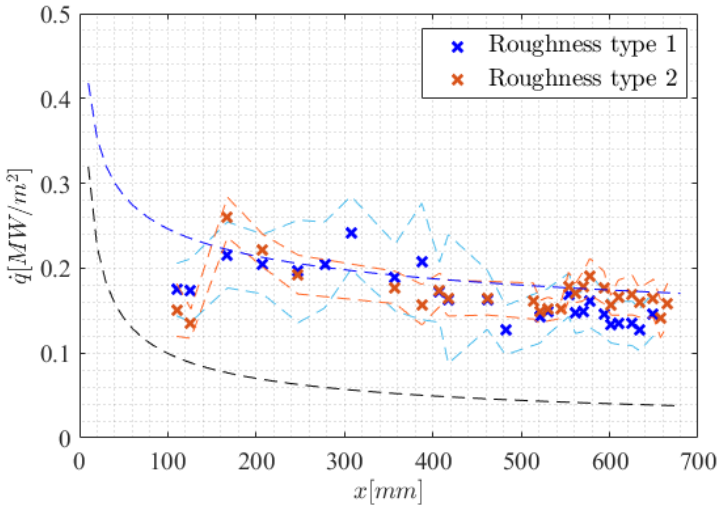

5-2 Mean surface heat flux along the centerline of the plate at $T_w = 300\ K$ with two different tyes of leading edge roughness. Standard deviation limits are indicated by the translucent dotted lines. The black and blue dotted lines correspond to the local laminar and turbulent surface heating as per the models of van Driest (1956).

Both roughness types increase the mean surface heat flux along the streamwise direction to that expected for a turbulent boundary layer. The final specifications of the roughness types are shown in table 5-1. These properties were extracted from the upstream laminar boundary layer based on nominal free-stream conditions with a heated flat plate.

5-1 Properties of the roughness elements used in this work. Laminar boundary layer heights and roughness Reynolds numbers are based on nominal free-stream conditions from CFD on a heated flat plate.

	Type 1	Type 2
k_{30} $[mm]$	1.01	0.60
δ_0 $[mm]$	3.0	3.0
k_{30}/δ_0	0.34	0.2
Re_{kk30}	2395	540

5.2.2. Effect of temperature

It was also required that the chosen roughness elements could induce a fully turbulent boundary layer at higher wall temperatures. The mean surface heat flux along the centerline is shown in figure 5-3 for roughness type 1. This was examined for a cold wall ($T_w = 300\ K$) and the heated wall at a maximum wall temperature of 714 K.

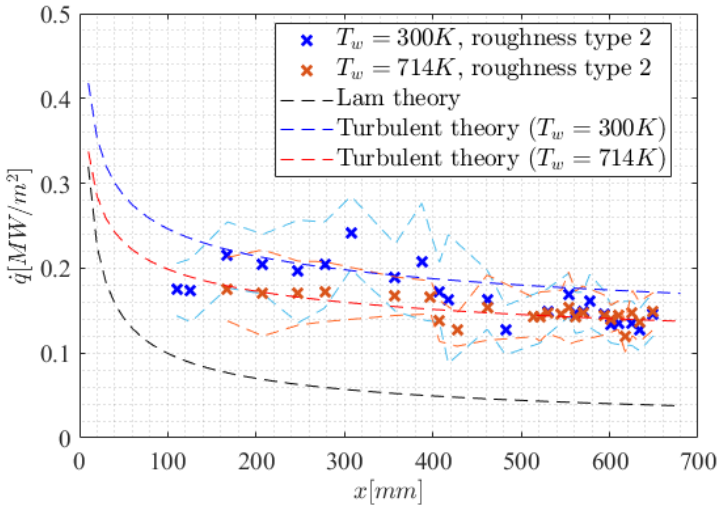

5-3 Mean surface heat flux along the centerline of the plate with roughness type 1 at $T_w = 300\ K$ and a maximum wall temperature of 714 K. Standard deviation limits are indicated by the translucent dotted lines. The solid black and blue dotted lines correspond to the local laminar and turbulent surface heating as per the models of van Driest (1956).

Figure 5-3 shows that the mean surface heat flux at the highest wall temperature is indicative of a turbulent boundary layer. The roughness type 1 was therefore concluded to be applicable to generating a turbulent boundary layer for the SWBLIs examined in this work.

5.3. SWBLIs

In order to verify baseline functionality of the model, transducers and testing procedures in the presence of large pressure gradients and heat fluxes due to an impinging shock, the examination of SWBLIs was undertaken incrementally. This was the first time that this type of configuration was tested at the HEG tunnel with a heated model, leading to a complex testing procedure.

5.3.1. Baseline tests

The mean centerline heat flux from baseline SWBLI tests are shown in figure 5-4 for an unheated wall at $T_w = 300\ K$. All curves are referenced to the same shock impingement point.

The impinging shock wave leads to a strong surface heat flux increase. If the shock is strong enough, the boundary layer separates. Separation is indicated by the increase of the surface heat-flux above the turbulent level of the incoming boundary layer. The start of separation for each case is shown in the zoomed-in view of figure 5-4. Maximum surface heat flux is obtained at reattachment of the separated flow onto the surface of the flat plate which increases with shock generator angle. Downstream of reattachment, the boundary layer undergoes a relaxation and surface heat flux reduces. This tends towards the turbulent level of the upstream boundary layer. Measurements in this region have been

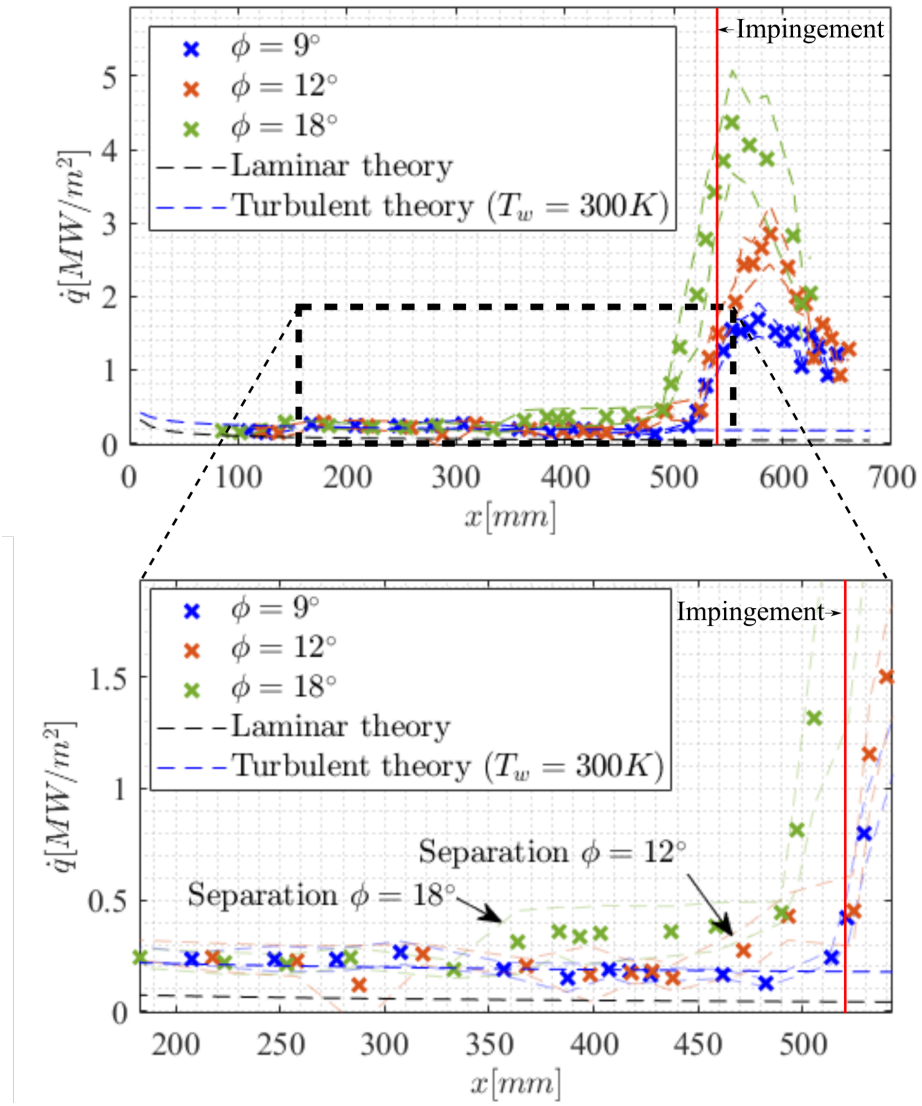

5-4 Mean surface heat flux along the centerline of the plate with roughness type 1 at a wall temperature of $T_w = 300\ K$. Shock generator angles were tested as shown in the figures. Standard deviation limits are indicated by the translucent dotted lines. The solid black and blue dotted lines correspond to the local laminar and turbulent surface heating as per the models of van Driest (1956). Top: overview of mean centerline heat flux. Bottom: zoomed-in view showing the start of separation for $\phi = 12°$ and $\phi = 18°$.

found to be useful for the comparison of LES and DNS modeling with experimental data (Volpiani et al., 2019).

Larger shock angles induce separation further upstream, as seen in the zoom of figure 5-4. For the case with an 18° shock generator angle, separation is induced 100 mm upstream compared to the case with a 12° shock generator angle. When the shock generator is reduced to an angle of 9°, the resulting adverse pressure gradient is not large enough to induce separation any more. In this case the heat flux increase is only due to the presence of the shock. Furthermore, the reduction of the heat flux due to relaxation occurs over a longer streamwise distance compared to when separation occurs with the shock generator at angles 12° and 18°.

5.3.2. Reynolds number effect

The effect of free-stream unit Reynolds number was examined with two different free-stream conditions with a shock generator angle of $\phi = 12^{\circ}$ with the same impingement location of the shock on the plate. The free-stream unit Reynolds numbers are shown in table 5-2. free-stream properties were obtained from the DLR-TAU non-equilibrium simulations of the nozzle used. The position of the model within the nozzle was accounted for when extracting free-stream properties. Furthermore, the variation in free-stream unit Reynolds number from the plate leading edge to the nozzle exit plane was found to be negligible.

5-2 free-stream Reynolds numbers for examining the effect of Reynolds number of the unheated SWBLI.

	Re_u $[\times 10^6\ m^{-1}]$	Max. variation to nozzle exit [%]
Condition A	4.04	2.2
Condition B	6.45	2.2

The mean surface heat flux and mean surface pressure were examined at the two different free-stream unit Reynolds numbers. Surface heat flux immediately downstream of separation was found to be only mimimally larger for the higher free-stream unit Reynolds number case. This increase of surface heat flux at separation is consistent with findings from the companion LES work of Volpiani et al. (2019) and with previous experimental findings from Schülein (2006) concerning turbulent SWBLIs. Peak surface heat flux during reattachment is found to be around $38\ \%$ higher for the higher free-stream unit Reynolds number case. The mean surface pressure data show a slightly different situation, in which there is a sharper increase in pressure at the start of separation for the higher free-stream unit Reynolds number case. Surface pressure at reattachment is also $55\ \%$ higher for the higher free-stream unit Reynolds number case. Mean surface heat flux and pressures were found to indicate separation and reattachment at the same streamwise locations on the flat plate.

The pressure spectra were obtained for two transducers (names PH08 and PH10) in the interaction region for both free-stream unit Reynolds numbers. PH08 is located at $x =$

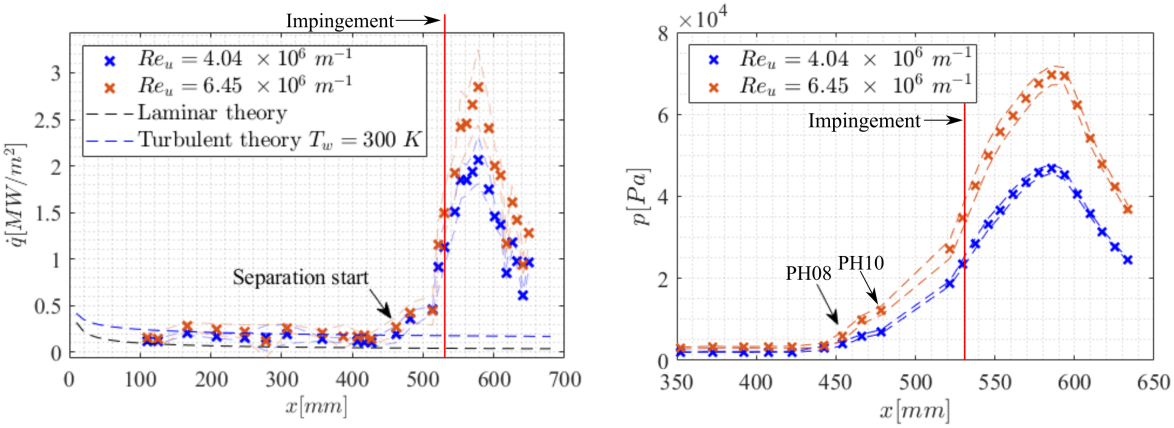

5-5 Comparison of surface measurements for two different free-stream unit Reynolds numbers with a shock generator angle of $\phi = 12°$. Left: Mean surface heat flux along the centerline of the plate. Right: Mean pressure along the centerline of the plate. Standard deviation limits are indicated by the translucent dotted lines. Separation is indicated by the arrow in each plot.

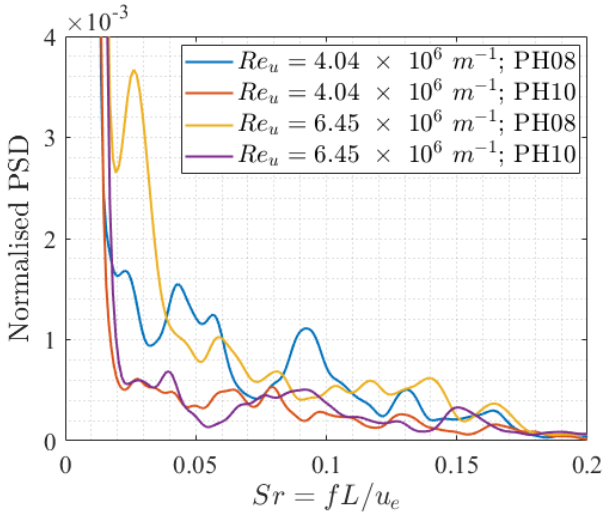

5-6 Pressure spectra of two pressure transducers in the interaction region. These were computed using Welch's method with 12-bit windows and 50 % overlap. PH08 is located at $x = 454.4\ mm$ and PH10 is located at $x = 478.4\ mm$

$454.4\ mm$ at the upstream portion of the interaction region. PH10 is located at $x = 478.4\ mm$ which is within the separation bubble region. The spectra are plotted against Strouhal number defined as per Dussauge et al. (2006):

$$Sr = \frac{fL}{u_e} \tag{5-1}$$

The spectra show the upstream region of the interaction region to contain higher energies at frequencies of about $2\ kHz$, corresponding to a Strouhal number in the range of $0.03 - 0.04$.L denotes the interaction length as defined above. The low-frequency energy content of the upstream portion of the interaction region is observed to be larger for the larger free-stream unit Reynolds number case. The presence of low-frequency content has undergone significant investigation at low supersonic Mach numbers, however, few studies have quantified this for hypersonic and higher-enthalpy flows Settles and Dodson (1994).

5.3.3. Heated SWBLIs

The main objective of this work was to investigate SWBLIs with a heated surface. This allows variation of the wall-to-free-stream temperature ratio (T_w/T_∞) independently of Mach- and Reynolds numbers. Based on the average reservoir properties (see table 4-3), three wall-to-recovery temperature ratios were investigated, namely: $T_w/T_\infty \approx 1.14$; $T_w/T_\infty \approx 2.40$; and $T_w/T_\infty \approx 2.70$. The wall-to-free-stream temperature ratio of 2.40 (maximum surface temperature of 633 K) was used as an intermediate step to minimize possible risk to model transducers in the presence of high heat flux from the heating element at the highest thermal operating condition i.e., for the wall-to-free-stream temperature ratio of 2.40 (maximum surface temperature of 714 K).

5.3.3.1. Flow organization

The overall organization of the flow can be inferred from schlieren recordings, as shown in figure 5-7, for the case of two different wall temperatures as indicated. These images were the result of averaging the image dataset over the steady flow time. The interaction length was found to be larger for increased wall-to-recovery temperature ratios, as indicated in figure 5-7. This proves that the wall heat transfer effect was considerable over the short test times of the HEG. The increase in interaction length with wall temperature is also in line with the work of Jaunet et al. (2014) for the low supersonic Mach number case detailed therein. Further insight into the flow can be obtained from the instantaneous schlieren images in figure 5-8.

The impinging shock waves are clearly shown. Donwstream at a shallower angle, the image of the diffracted part of the impinging shock is displayed. These three-dimensional portions of the impinging shock were found to not affect the measurements on the centerline of the plate and within the field of depth of the focused schlieren system. The impinging shock is able to be traced up until $y/\delta_0 \approx 0.53$ for the unheated case, while this value increases to $y/\delta_0 \approx 0.83$ for the heated case. This indicates that the sonic line within the interaction increases in wall-normal height relative to the incoming boundary layer height. This is in

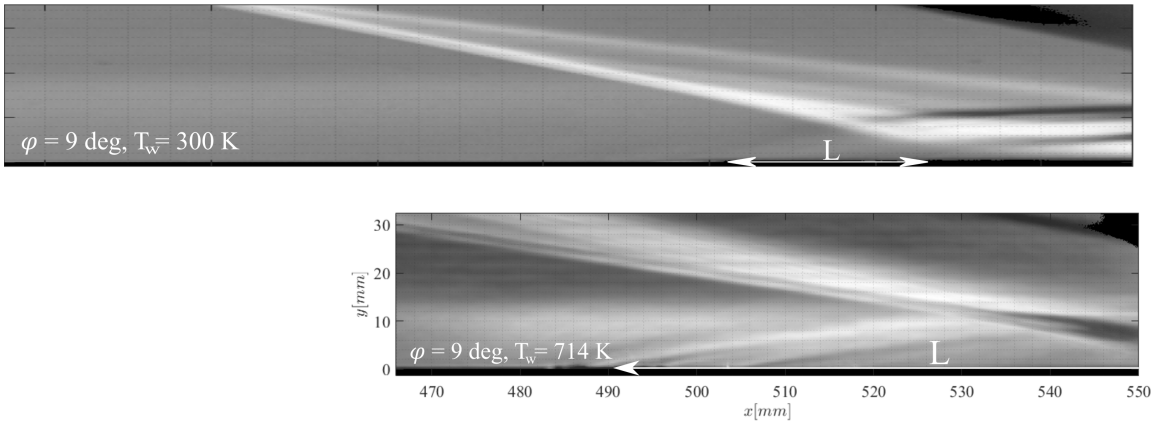

5-7 Mean flow organization with different wall temperatures and a shock generator angle of $\phi = 9°$. A standard schlieren setup was used for the unheated case ($T_w = 300\ K$) while the focused schlieren setup was used for the heated case with $T_w = 714\ K$.

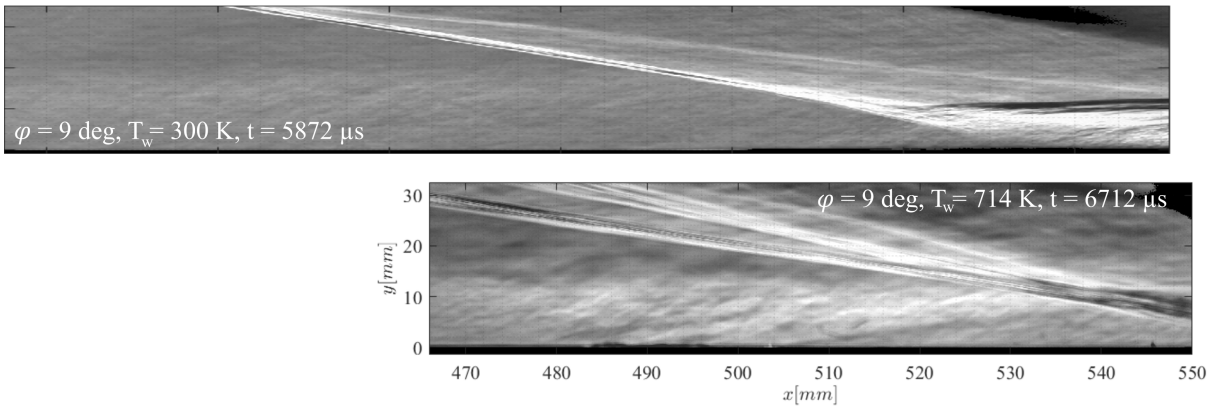

5-8 Instantaneous schlieren frames of the SWBLI with different wall temperatures and a shock generator angle of $\phi = 9°$. A standard schlieren setup was used for the unheated case ($T_w = 300\ K$) while the focused schlieren setup was used for the heated case with $T_w = 714\ K$.

line with the PIV results of Jaunet et al. (2014) and DNS simulations of Bernardini et al. (2016) reported for varying wall-to-recovery temperature ratios.

5.3.3.2. Mean surface heat flux

The wall heat flux was determined from the thermocouples placed on the centerline of the heated and unheated portions of the flat plate. Additionally, there were thermocuples on the spanwise coordinate of the unheated portion at $y = 32\ mm$. The mean surface heat flux for all thermocouples is shown in figure 5-9. Cases with a shock generator angle of $\phi = 12°$ (left column) and $\phi = 18°$ (right column) are presented. The abscissa are normalised with the incoming turbulent boundary layer height relative to the inviscid impingement location x_{imp}. Boundary layer heights were determined from the schlieren images. Higher wall-to-recovery temperature ratio cases resulted in larger normalised distances from separation onset to maximum mean surface heat flux. This is denoted as $\Delta_x q$ and is shown in table 5-3.

5-3 Normalised distances from separation onset to maximum mean surface heat flux along the centerline (denoted Δ_{xq}) for $\phi = 12°$ and $\phi = 18°$.

T_w/T_∞	Δ_{xq} for $\phi = 12°$	Δ_{xq} for $\phi = 18°$
1.14	6.2	10.15
2.40	8.11	10.48
2.70	8.07	11.49

From the zoomed-in views of figure 5-9, the effect of increasing wall-to-recovery temperature resulted in a shallower increase in mean surface heat flux donwstream of separation. Notably, the relaxation donwstream of peak heat flux and during reattachment is also less immediate for higher wall-to-recovery temperature ratios. Relaxation is therefore delayed for higher wall-to-recovery temperature ratios and is an important result given the uncertainty and sensitivity of Stanton number calculated in this region for DNS and LES computations (Volpiani et al., 2019).

The spanwise thermocouples on the unheated portion show a similar trend, with delayed relaxation for higher wall-to-recovery temperature ratios. However, relaxation is more immediate given the shorter streamwise extents of the separation bubble in the off-center regions Gaitonde (2015); Rabey et al. (2019).

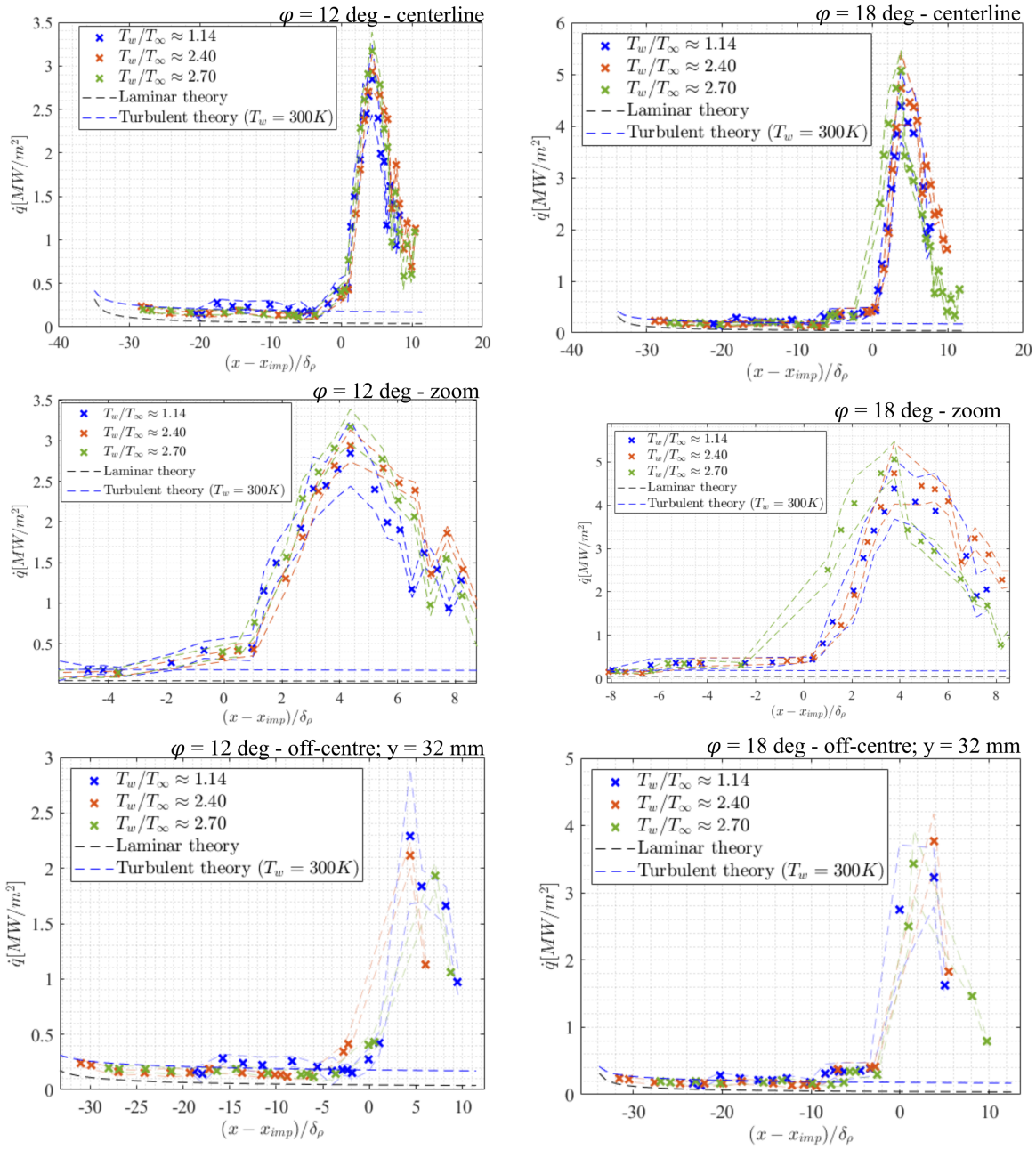

5-9 Mean centerline and mean off-centre surface heat flux for cases with $\phi = 12°$ (left column) and $\phi = 18°$ (right column). All data are anchored to the reattachment point, determined by maximum surface heat flux. The top row shows mean surface heat flux from thermocouples on the centerline of the flat plate model. The middle row shows a zoomed-in view around the start of seperation up until the region of maximum surface heat flux. The bottom row shows the centerline heat flux from thermocuples on the centerline as well as from thermocouples on the spanwise coordinate $y = 32\ mm$ on the unheated portion. Dashed lines near the symbols show single standard deviation limts.

5.3.3.3. Mean surface pressure

The surface pressure on the centerline of the heated and unheated portions of the flat plate. Additionally, there were pressure transducers on the spanwise coordinate of the unheated portion at $y = 47\ mm$. The mean surface pressure for all aforementioned pressure transducers is shown in figure 5-10. Cases with a shock generator angle of $\phi = 12°$ (left column) and $\phi = 18°$ (right column) are presented. The abscissa are normalised with the incoming turbulent boundary layer height (density gradient-based) relative to the inviscid impingement location x_{imp}. Pressures are normalised with the free-stream pressure obtained from upstream transducers on the flat plate.

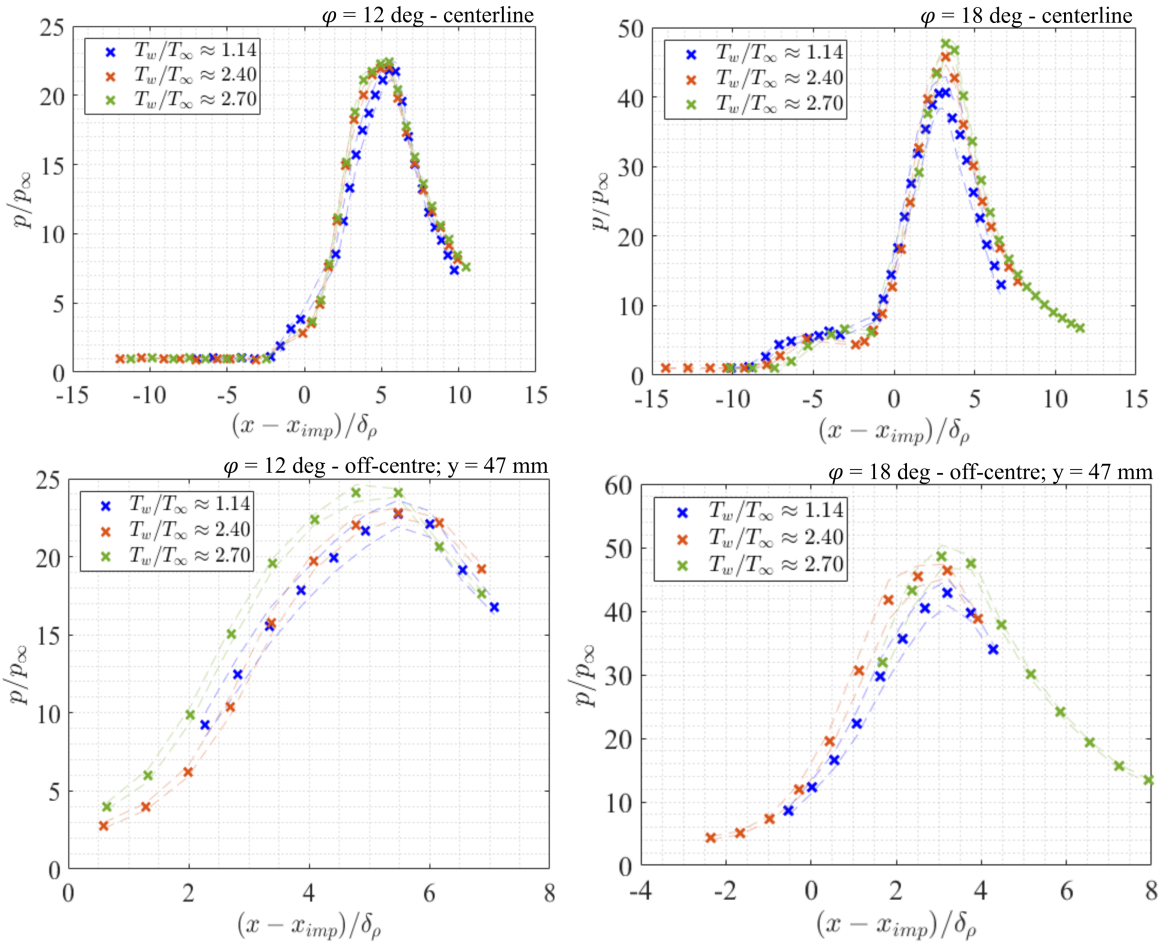

5-10 Mean centerline and mean off-centre surface pressure for cases with $\phi = 12°$ (left column) and $\phi = 18°$ (right column). All data are anchored to the reattachment point, determined by maximum surface pressure. The top row shows mean surface heat flux from high-temperature resistant Kulites and GE pressure transducers on the centerline of the flat plate model. The bottom row shows only the GE pressure transducers on the spanwise coordinate $y = 47\ mm$ on the unheated portion. Dashed lines near the symbols show single standard deviation limts.

Normalized distances from separation onset to maximum mean surface pressure do not vary as much with wall temperature variation, compared to what was shown above for mean surface heat flux. Furthermore, the relaxation region downstream of maximum

mean surface pressure (accompanied by the decrease in surface pressure) was found to have the same slope independent of surface temperature. This was also observed for the pressure transducers on the spanwise station at $y = 47\ mm$. The increase of wall temperature was found to increase the maximum mean surface pressure.

5.3.3.4. Surface pressure spectra

Low-frequency unsteadiness has been known for a long time to be a property of SWBLIs. This is briefly included here for the shock generator angles of $\phi = 9°$ and $\phi = 12°$. Figure 5-11 shows these two cases with varying wall temperatures. Pressure transducers PH08 and PH10 were chosen for investigation into dominant low-frequency pressure fluctuations. These were located on the heated portion of the flat plate. PH10 was not available for all tests discussed here. The locations of the transducers PH08 and PH10 relative to the interaction region of the SWBLI are displayed in the legends of each figure. For the $\phi =$

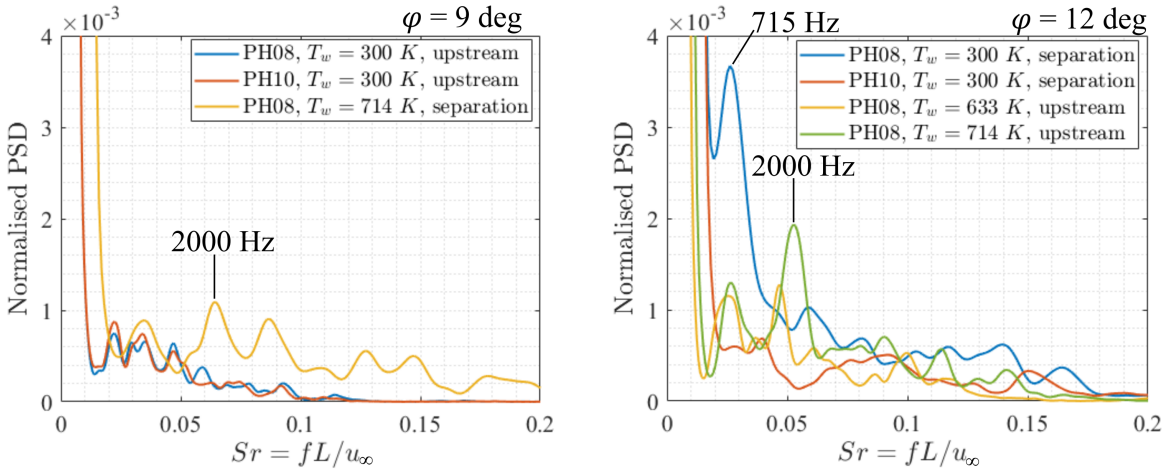

5-11 Strouhal number defined as per equation 5-1 for high-temperature-resistant Kulite pressure transducers located around the interaction region. Relation of the transducers to the interaction region is indicated in each figure. Shock generator angles of $\phi = 9°$ (left) and $\phi = 12°$ (right) are shown.

$9°$ case, the low-frequency energy content is only seen to increase within the separation region and a peak at $2000\ Hz$ or $Sr = 0.065$ was observed. Some broadband content was also displayed. This was in contrast to the case with an increased shock generator angle of $\phi = 12°$. Within the separation region, a low frequency peak was observed at $715\ Hz$ or $Sr = 0.025$ for PH08 at $T_w = 300\ K$. Downstream within the separation region this frequency content is sharply reduced, probably due to higher frequencies emerging due to reattachment of the turbulent boundary layer. The low frequency content was found to increase, the closer PH08 was to being located within the separation region. For the cases with $T_w = 633\ K$ and $T_w = 714\ K$, the location of PH08 was brought closer to separation with increasing wall temperature due to the increase in separation size. The low-frequency peak at $2000\ Hz$ was observed to increase with wall temperature. The peak at around $700\ Hz$ was also observed to emerge as temperature was increased. Higher frequency content is also observed to increase with increasing wall temperature, and was seen for both shock generator angles.

6. Conclusion

Shock wave/boundary layer (SWBLI) experiments in a hypersonic flow with highly cooled walls at varying wall-to-freestream temperature ratios were successfully carried out at the High Enthalpy Shock Tunnel Göttingen (HEG). Various efforts were made to ensure coordination of the experimental work with numerical work carried out by Volpiani et al. (2019). It was concluded that the current experiments enable exploration of cooled-wall hypersonic SWBLI phenomena in combination with the work undertaken by Professor Johan Larsson of University of Maryland (USA) within his AFOSR grant on 'The effects of strong wall cooling on supersonic and hypersonic shock/boundary-layer interactions'. Further detailed scientific conclusions are listed in the following paragraphs.

A natural turbulent boundary layer was not able to be produced on the current flat plate model at the largest freestream unit Reynolds number condition tested at the HEG. This necessitated artificially tripping of the boundary layer. Two leading edge roughness types were tested based on preliminary experiments. Both types were found to produce fully turbulent boundary layers, based on mean surface heat flux criteria. Stochastic interspersed gravel was used for most tests, based on its reduced roughness height and consequently reduced disturbances imparted to the freestream.

Baseline SWBLI experiments were conducted at unheated wall conditions ($T_w = 300\ K$) to assess the effect of shock angle and freestream unit Reynolds number on mean surface heat flux and pressure. Three shock generator angles were tested: $\phi = 9°$ to $\phi = 12°$ and $\phi = 18°$. It was found that increases in shock angle produced larger separation region sizes as observed in both heat flux and pressure data. This supported the LES data of the companion project. Two freestream unit Reynolds numbers were tested: $Re_u = 6.45 \times 10^6 m^{-1}$ (Condition A) and $Re_u = 4.04 \times 10^6 m^{-1}$ (Condition B). The increased freestream unit Reynolds number did not shift separation location, but increased the pressure within the separation region.

The effect of wall temperature was assessed by heating the flat plate surface to temperatures of $T_w = 633\ K$ and $T_w = 714\ K$. Various wall-to-freestream temperature ratios were tested: $T_w/T_\infty \approx 1.14$; $T_w/T_\infty \approx 2.40$; and $T_w/T_\infty \approx 2.70$. The increase in wall-to-freestream temperature ratio was found to increase the SWBLI interaction length, which was visible in schlieren and focused schlieren images even for the smallest shock generator angle. This was supported by the LES observations.

Relaxation of the mean surface heat flux was found to occur over shorter streamwise extents downstream of reattachment for higher wall-to-freestream temperature ratios. This supports the LES work and is critical to reducing numerical uncertainties. Spanwise mean

surface heat flux shows a different state of relaxation and is important to modelling three-dimensional SWBLIs. Mean surface pressure did not exhibit drastically different relaxation rates downstream of reattachement for all wall-to-temperature ratios. This was also concluded from spanwise transducers.

A limited investigation of unsteadiness within the separation region was also conducted. This showed that the increase in shock generator angle and consequently larger separation region shifted the higher energy peaks of the pressure spectra to lower frequencies. Furthermore, transducers placed in the upstream portion of the separation region detected increased low-frequency content at $Sr = 0.03$, which was also noted for certain supersonic SWBLI experiments.

Further work on this topic (not included within the scope of this Grant) will be focused on further RANS computations to match the tripped boundary layer height observed during experiments. This will enable further specification of the boundary layer state to assist experimental condition-specific LES computations and comparisions.

7. Attachment

10/00

DESIGN YOUR OWN MEDTHERM CO-AX METAL WALL SURFACE TEMPERATURE PROBE

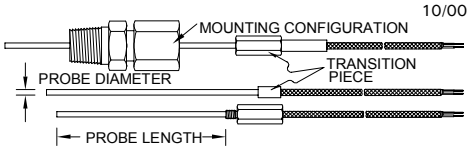

1

SELECT PROBE DIAMETER, PROBE MATERIAL (ISA CALIBRATION), AND PROBE LENGTH. Start all surface temperature probe model numbers with TCS, then add the code for probe diameter, and the ISA Calibration symbol, and add the probe length in inches (tolerance on probe length is ±.010"). If a .061 diameter "K" (chromel/alumel) probe, 1.00" long is desired, start the model designation as TCS-061-K-1.00

*Price for additional length is determined by the length to the nearest 1/2".

ISA Calibration	LENGTH Inches	Basic price for 0-1" probe length	Price for each Additional inch
.015" ± .001" Probe Dia. (Code 015)			
E	0-6		
K	0-6		
S	0-6		
.031" ± .001" Probe Dia. (Code 031)			
T	0-6		
J	0-6		
E	0-6		
K	0-6		
S	0-6		
.061" ± .001" Probe Dia. (Code 061)			
T	0-6		
J	0-6		
E	0-6		
K	0-6		

ISA Calibration	LENGTH Inches	Basic price for 0-1" probe length	Price for each Additional inch
.099" ± .001" Probe Dia. (Code 099)			
T	0-6		
J	0-6		
E	0-6		
K	0-6		
#3-56 Thread Full Length of Probe (Code 099T)			
T	0-1		
J	0-1		
E	0-1		
K	0-1		

2

SELECT JUNCTION PLATING MATERIAL. Recommended platings are shown in table at extreme right. Add the plating code to the model number. If chromium plating is desired, add - CR to the model number; TCS-061-K-1.00-CR.

Available Plating Materials		
Material	Order Code	Price
None	0	
Chromium	CR	
Nickel	NI	
Platinum	PT	
Copper	CU	

Recommended Plating Materials	
ISA Calibration Code	Plating Material
T	CR
J	CR
E	CR
K	CR
S	PT

3

SELECT LEAD WIRE INSULATION AND LENGTH OF LEADS. Add the insulation code to the model number. All lead wires are 28 or 30 AWG (factory selects the largest lead possible with each probe). Standard lead wire length is one foot and is included in the basic price of the probe. If more than one foot lead length is desired, add the number of whole feet to the insulation code. If fiberglass primary and fiberglass secondary insulation, metallic braided shielding and two feet of lead wire are desired, add GGS2 to the model number; TCS-061-K-1.00-CR-GGS2.
(Teflon usable to 220ºC, Fiberglass usable to 500ºC, one time to 700ºC.)

Primary	Secondary	Order Code	Price for each foot over the one ft. std.
Fiberglass	Fiberglass	GG	
Teflon	Fiberglass	TG	
*Fiberglass	Fiberglass	GGS	
*Teflon	Fiberglass	TGS	

*Metallic braided shielding overall.

4

SELECT TRANSITION PIECE. Add the transition piece code to the model number. Example: If a 1/4" hex filled with ceramic and a strain relief tube are desired, add B2CSR to model number; TCS-061-K-1.00-CR-GGS2-B2CSR.

Description		Code	Price
Cylindrical Transition, Stainless Steel, Epoxy filled (175ºC)	.187" dia. x 3/4" lg	A1	
	.125" dia. x 1/4" lg	A2	
	.093" dia. x 1/4" lg	A3	
Hex Transition, Stainless Steel, Epoxy filled(175ºC)	3/16"Hex x 1/2" lg.	B1	
	1/4"Hex x 1/2" lg.	B2	
	3/8"Hex x 3/4" lg.	B3	
	1/4"Hex x 3/8" lg.	B4	

Optional Features		
Description	Add to Code	Add to Price
Ceramic Filled, (With fiberglass wire only, useful to 700ºC,see wire temp. limits)	C	
Strain Relief Tube (Available on "B" hex transitions only)	SR	

5

SELECT MOUNTING CONFIGURATION. Add code to model number (if mounting provisions not required, use order code "0"). If a variable immersion type with 1/8" NPT mountingthread is desired, add -BB to model number; TCS-061-K-1.00-CR-GGS2-B2CSR-BB.

Threaded Section on Front of Transition Piece. (Use with B1, B2, B3, or B4 Hex Transition only)				
Hex Size	Thread	Thread Length	Code	Price
3/16"	#3-56UNF	1/8"	AA	
1/4"	#3-56UNF	1/2"	AB	
3/8"	1/4-28UNF	1"	AC	
1/4"	#8-32UNC	1/4"	AD	

SST Variable Immersion Fitting with Lava Gland * (1/8-NPT to 7500 psi and 1/16-NPT to 5000 psi.)					
Probe Code	NPT	Hex	Max. Length	Code	Price
015 or 031	1/16"	11/32"	0.90"	BAA	
061	1/16"	11/32"	0.90"	BA	
015 or 031	1/8"	1/2"	1.25"	BBA	
061	1/8"	1/2"	1.25"	BB	
099	1/8"	1/2"	1.25"	BC	

* To specify Teflon gland (220ºC max), add "T" to Code.

EXAMPLE

Suppose that a chromel-alumel probe with chromium plating is desired; the probe diameter is to be .061", the probe length is to be 1.00", the lead wire is to have fiberglass on each wire and fiberglass overall with a metallic braid shielding, a 1/4" hexagonal transition piece will house the junction of the lead wire to the probe, with ceramic potting, strain relief tube, and a 1/16" NPT variable immersion type fitting is to be installed on the probe (same as example used in steps 1 through 5, above).
The probe and its Model Number designation are shown below:

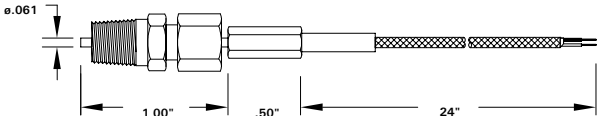

Model Code	1 Probe Diameter Code	1 ISA Calibration Code	1 Probe Length Code	2 JunctionPlating Material Code	3 Insulation Code	3 Lead Length Code	4 Transition Piece Code	4 Ceramic Code	4 Strain Relief Code	5 Mounting Configuration Code
TCS	061	K	1.00	CR	GGS	2	B2	C	SR	BA

Model TCS-061-K-1.00-CR-GGS2-B2CSR-BA:

7-1 Specification sheet of coaxial thermocouple type E.

kulite®

SUPER HIGH TEMPERATURE IS® PRESSURE TRANSDUCER

XTEH-10L-190 (M) SERIES

- –65°F To 1000°F Temperature Capability*
- Patented Leadless Technology **VIS**®
- High Natural Frequency
- Suitable For Stall Avoidance Application

The XTEH Series pressure transducers feature a very wide operating temperature range. These characteristics make these devices ideal for Turbine engine testing especially in the areas of stall avoidance and active stability control. Other equally demanding applications in the industry may also benefit from the ruggedness of these devices.

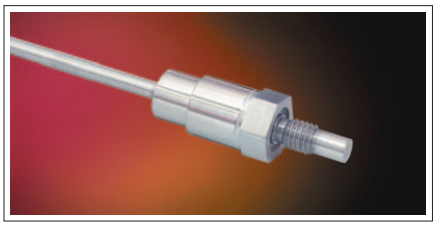

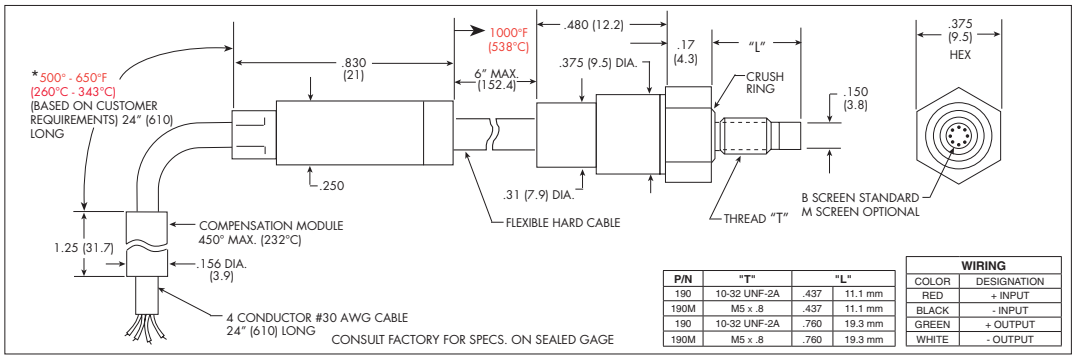

P/N	"T"	"L"	
190	10-32 UNF-2A	.437	11.1 mm
190M	M5 x .8	.437	11.1 mm
190	10-32 UNF-2A	.760	19.3 mm
190M	M5 x .8	.760	19.3 mm

WIRING	
COLOR	DESIGNATION
RED	+ INPUT
BLACK	- INPUT
GREEN	+ OUTPUT
WHITE	- OUTPUT

INPUT Pressure Range	1.7 25	3.5 50	7 100	14 200	21 300	35 500	70 1000	140 2000	210 BAR 3000 PSI
Operational Mode	Absolute, Sealed Gage								
Over Pressure	2 Times Rated Pressure								
Burst Pressure	3 Times Rated Pressure								
Pressure Media	All Nonconductive, Noncorrosive Liquids or Gases (Most Conductive Liquids and Gases - Please Consult Factory)								
Rated Electrical Excitation	10 VDC/AC								
Maximum Electrical Excitation	15 VDC/AC								
Input Impedance	1000 Ohms (Min.)								
OUTPUT Output Impedance	1000 Ohms (Nom.)								
Full Scale Output (FSO)	100 mV (Nom.)								
Residual Unbalance	± 5 mV (Typ.)								
Combined Non-Linearity, Hysteresis and Repeatability	± 0.1% FSO BFSL (Typ.) ± 0.5% FSO (Max.)								
Resolution	Infinitesimal								
Natural Frequency (KHz) (Typ.)	240	300	380	500	575	700	1000	1400	1650
Acceleration Sensitivity % FS/g Perpendicular Transverse	$5.0x10^{-4}$ $6.0x10^{-5}$	$3.0x10^{-4}$ $4.0x10^{-5}$	$1.5x10^{-4}$ $2.0x10^{-5}$	$1.1x10^{-4}$ $1.5x10^{-5}$	$9.0x10^{-5}$ $1.0x10^{-5}$	$6.5x10^{-5}$ $7.0x10^{-6}$	$4.0x10^{-5}$ $4.0x10^{-6}$	$2.5x10^{-5}$ $3.0x10^{-6}$	$1.9x10^{-5}$ $2.0x10^{-6}$
Insulation Resistance	100 Megohm Min. @ 50 VDC								
ENVIRONMENTAL Operating Temperature Range	-65°F to +1000°F* (-55°C to +538°C) - Cable Area								
Compensated Temperature Range	+80°F to +850°F (+25°C to +454°C)								
Thermal Zero Shift	± 1.5% FS/100°F (Typ.)								
Thermal Sensitivity Shift	± 1.5% /100°F (Typ.)								
Steady Acceleration and Linear Vibration	1,000g. Sine								
PHYSICAL Electrical Connection	4 Conductor 30 AWG Shielded Cable (24" After Module)								
Weight	8 Grams (Nom.) Excluding Cable								
Pressure Sensing Principle	Fully Active Four Arm Wheatstone Bridge Dielectrically Isolated Silicon on Silicon Patented Leadless Technology								
Mounting Torque	15 Inch-Pounds (Max.) 1.7 N-m								

** Limited life above 850°F (455°C), dependent on operating conditions.*
Note: Custom pressure ranges, accuracies and mechanical configurations available. Dimensions are in inches. Dimensions in parenthesis are in millimeters.
Note: Requires external compensation module (Max. temp. 450°F) Please refer to outline drawing.
Continuous development and refinement of our products may result in specification changes without notice - all dimensions nominal. (N)

KULITE SEMICONDUCTOR PRODUCTS, INC. • One Willow Tree Road • Leonia, New Jersey 07605 • Tel: 201 461-0900 • Fax: 201 461-0990 • http://www.kulite.com

7-2 Specification sheet of high temperature KULITE pressure transducer.

Bibliography

H. Babinsky and J. K. Harvey, editors. Shock wave-boundary-layer Interactions. Cambridge University Press, 2011.

E. Schülein. Effects of laminar-turbulent transition on the shock-wave/boundary-layer interaction. In 44th AIAA Fluid Dynamics Conference, 2014.

C. H. Law. Supersonic shock wave turbulent boundary-layer interactions. AIAA Journal, 14 (4):730–734, 1976.

C. C. Horstman. Hypersonic shock-wave/turbulent-boundary-layer interaction flows. AIAA Journal, 30(6):1480–1481, 1992.

N. D. Sandham, E. Schülein, A. Wagner, S. Willems, and J. Steelant. Transitional shock-wave/boundary-layer interactions in hypersonic flow. Journal of Fluid Mechanics, 752: 349–382, jul 2014. doi: 10.1017/jfm.2014.333.

M. S. Holden. Shock wave-turbulent boundary layer interaction in hypersonic flow. In 10th Aerospace Sciences Meeting. American Institute of Aeronautics and Astronautics, January 1972. doi: 10.2514/6.1972-74.

M. Holden. A study of flow separation in regions of shock wave-boundary layer interaction in hypersonic flow. In 11th Fluid and PlasmaDynamics Conference, page 1169, 1978.

J. E. Lewis, T. Kubota, and L. Lees. Experimental investigation of supersonic laminar two-dimensional boundary layer separation in a compression corner with and without cooling. In AIAA 5th Aerospace Scienses Meeting, 1967.

M. Bleilebens and H. Olivier. On the influence of elevated surface temperatures on hypersonic shock wave/boundary layer interaction at a heated ramp model. Shock Waves, 15 (5):301–312, 2006.

F. Scortecci, F. Paganucci, and L. dAgostino. Experimental investigation of shock wave/boundary layer interactions over an artificially heated model in hypersonic flow. In 8th AIAA International Space Planes and Hypersonic Systems and Technologies Conference. American Institute of Aeronautics and Astronautics, April 1998. doi: 10.2514/6.1998-1571.

P. S. Volpiani, A. Wagner, M. Bernardini, and J. Larsson. Using large-eddy simulations to design a new hypersonic shock/boundary-layer interaction experiment. In AIAA Scitech 2019 Forum. American Institute of Aeronautics and Astronautics, Jan 2019. doi: 10.2514/6.2019-0098.

D. C. Reda. Correlation of nosetip boundary layer transition data measured in ballistic-range experiments. AIAA Journal, 19:329–339, March 1981.

R. G. Batt and H. H. Legner. A review of roughness-induced nosetip transition. AIAA Journal, 21(1), 1983. doi: 10.2514/3.60102.

D. C. Reda. Review and synthesis of roughness-dominated transition correlations for reentry applications. Journal of Spacecraft and Rockets, 39(2):161–167, March-April 2002.

G. S. Settles. Schlieren and Shadowgraph Techniques: Visualizing Phenomena in Transparent Media, volume ISBN: 3-540-66155-7. Springer Berlin Heidelberg, 2001.

L.M. Weinstein. Review and update of lens and grid schlieren and motion camera schlieren. The European Physical Journal Special Topics, 182(1):65–95, apr 2010. doi: 10.1140/epjst/e2010-01226-y.

Leonard M. Weinstein. Large-field high-brightness focusing schlieren system. AIAA Journal, 31(7):1250–1255, jul 1993. doi: 10.2514/3.11760.

A. Mack and V. Hannemann. Validation of the unstructured DLR-TAU-Code for hypersonic flows. In 32nd AIAA Fluid Dynamics Conference and Exhibit, 2002. AIAA 2002-3111.

E. R. van Driest. The problem of aerodynamic heating. In Aeronautical Engineering Review, pages 26–41, October 1956.

E. Schülein. Skin friction and heat flux measurements in shock/boundary layer interaction flows. AIAA Journal, 44(8):1732–1741, August 2006. doi: 10.2514/1.15110.

J. P. Dussauge, P. Dupont, and J. F. Debiève. Unsteadiness in shock wave boundary layer interactions with separation. Aerospace Science and Technology, 10(2):85–91, March 2006. doi: 10.1016/j.ast.2005.09.006.

G. S. Settles and L. J. Dodson. Supersonic and hypersonic shock/boundary-layer interaction database. AIAA Journal, 32(7):1377–1383, July 1994. doi: 10.2514/3.12205.

V. Jaunet, J. F. Debieve, and P. Dupont. Length scales and time scales of a heated shock-wave/boundary-layer interaction. AIAA Journal, 52(11):2524–2532, 2014.

M. Bernardini, I. Asproulias, J. Larsson, S. Pirozzoli, and F. Grasso. Heat transfer and wall temperature effects in shock wave turbulent boundary layer interactions. Physical Review Fluids, 1(8):084403, December 2016. doi: 10.1103/physrevfluids.1.084403.

D. V. Gaitonde. Progress in shock wave/boundary layer interactions. Progress in Aerospace Sciences, 72:80–99, jan 2015. doi: 10.1016/j.paerosci.2014.09.002.

P. K. Rabey, S. P. Jammy, P. J. K. Bruce, and N. D. Sandham. Two-dimensional unsteadiness map of oblique shock wave/boundary layer interaction with sidewalls. Journal of Fluid Mechanics, 871, May 2019. doi: 10.1017/jfm.2019.404.